ABSTRACT

HOSANGADI, PRANAV. Improved Stall Prediction for Swept Wings Using Low-Order Aerodynamics. (Under the direction of Dr. Ashok Gopalarathnam.)

Low-order aerodynamic prediction methods are well-established in predicting the force and moment characteristics of arbitrary wing geometries at low angles of attack. Approaches to augment these methods by modeling flow separation at high angles of attack using an effective reduction in the camber show promise. These methods assume locally two-dimensional flow, and use airfoil characteristics to calculate the decambering corrections at high angles of attack. However, in the case of swept wings, a transverse pressure gradient induces a spanwise component in the flow over the wing. This flow transports the separated boundary layer from the root towards the tip. As a result of the disruption of the boundary layer at the outboard sections, separation occurs at smaller angles of attack than seen on unswept wings. The motion of the separated boundary layer away from the inboard sections allows the flow there to remain attached upto higher angles of attack. This non-uniform change in the separation behavior, and hence stall characteristics of the wing sections causes a breakdown of the assumptions used in the decambering approach. As a result, applying airfoil characteristics to sections of swept wings yields poor predictions for the lift curves.

A database of Reynolds-Averaged Navier-Stokes (RANS) CFD solutions was previously developed using NASA's TetrUSS CFD Package by the NCSU Applied Aerodynamics Lab for various airfoil and wing shapes. The current effort, described in this thesis, focuses on the obtaining corrections to the airfoil lift curve using the modified section characteristics of swept wings from the database. When these modified lift curves are used as section characteristics in the decambering method, the results match remarkably well with CFD predictions. This indicates that the strip-theory approach used in the decambering method is applicable swept wings, provided the effect of spanwise redistribution of flow-separation is accounted for. This success motivates research towards the development of a fully predictive low-order method.

Improved Stall Prediction for Swept Wings Using Low-Order Aerodynamics

by

Pranav Hosangadi

A thesis submitted to the Graduate Faculty of
North Carolina State University
in partial fulfillment of the
requirements for the Degree of
Master of Science

Aerospace Engineering

Raleigh, North Carolina

2015

APPROVED BY:

Dr. Jack Edwards	Dr. Venkateswaran Narayanaswamy

Dr. Ashok Gopalarathnam
Chair of Advisory Committee

DEDICATION

To my parents, late nights, the Rule of Three, and irony.

BIOGRAPHY

Pranav Hosangadi was born on April 15th, 1992 in Mumbai, India. He received his Bachelor's degree in Mechanical Engineering from the University of Mumbai in May 2013. Pranav enrolled at North Carolina State University in the Fall of 2013 to pursue a Masters degree in Aerospace Engineering, and joined the Applied Aerodynamics Lab under the guidance of Dr. Ashok Gopalarathnam shortly thereafter. Pranav will pursue a Ph.D. at NCSU upon completion of his Masters.

ACKNOWLEDGEMENTS

Foremost, I would like to express my gratitude to Dr. Ashok Gopalarathnam for his patience, advice and support over the past two years. His guidance was essential in the successful completion of this thesis. I am also grateful to Dr. Jack Edwards and Dr. Venkateswaran Narayanaswamy for the time they dedicated to serving on my committee. Thank you especially to our graduate services coordinator, Annie Erwin, for her help in all administrative matters.

I would also like to thank NASA Langley and the National Institute of Aerospace for funding my graduate research, and acknowledge the support and collaboration of Gautam Shah of NASA Langley, the technical monitor for this project, and the contributions of Neal Frink of NASA Langley and former NCSU graduate students Justin Petrilli and Kristen Patrick to earlier aspects of this research.

Thanks are also due to Ryan Paul for his invaluable insight and encouragement over the past year. To my other labmates: Aditya, Rajmohan, Shreyas, Vishnu, and Yoshi, thank you for the friendship and camaraderie.

Finally, thanks to my family for their love and support. You are the wind beneath my wings!

TABLE OF CONTENTS

LIST OF FIGURES

NOMENCLATURE

α	Angle of attack
α_{0L}	Zero-lift angle of attack
$\mathit{Æ}$	Aspect Ratio
C_D	Wing drag coefficient
C_d	Section drag coefficient
C_L	Wing lift coefficient
C_l	Lift Coefficient
C_l	Section lift coefficient
C_M	Wing moment coefficient
C_m	Section moment coefficient
f	Chordwise location of separation point, normalized by chord.
Re	Reynolds Number

Chapter 1

Introduction

Aircraft typically operate in the "linear region" of aerodynamics: the lift generated is linearly related to the angle of attack of the aircraft. The linearity of the lift curve is because the boundary layer is attached and thin, and the flow can be approximated to potential flow. This relationship has been thoroughly studied and extensive data is available for operation in this linear region from a variety of experimental, numerical, and theoretical sources for a variety of airfoil and wing geometries.

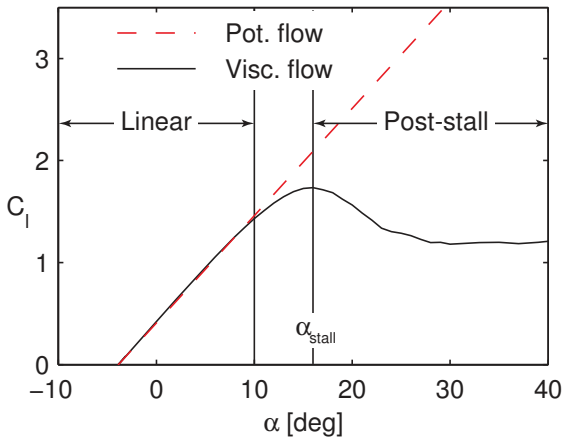

Figure 1.1: The linear and post-stall regions.

As the angle of attack, α is increased, however, the increasing adverse pressure gradient induces the separation of the boundary layer. A separated boundary layer is no longer thin enough to allow the flow to be approximated to an inviscid flow, and the actual lift curve is no longer linear. If the angle of attack is increased further, the lift curve peaks and then begins to fall. This peak angle is known as the stall angle (α_{stall}), and the post-stall regime comes into play at angles of attack higher than the stall angle.

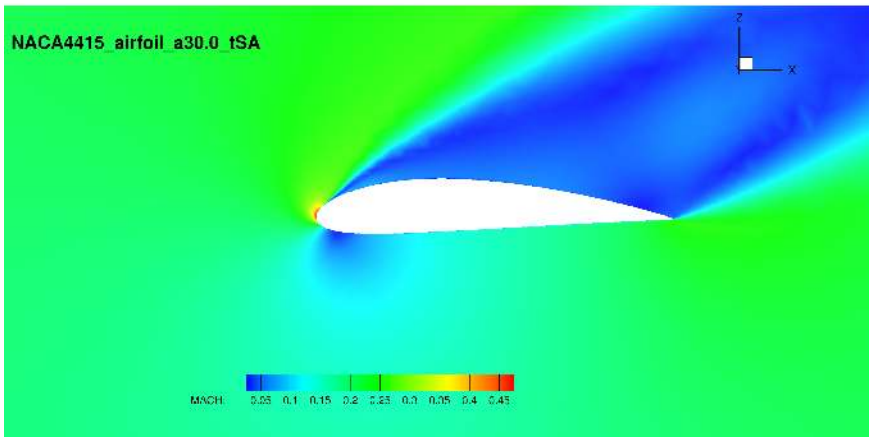

Figure 1.2: NACA 4415 airfoil at $\alpha = 30°$. This α is much greater than α_{stall}, and there is a large amount of separation over the upper surface.

1.1 Importance of studying post-stall aerodynamics

As discussed above, a majority of applications make use of the linear regime, which has been extensively studied and for which there exists a large repository of data. However, for certain applications, such as wind turbines, helicopters, and even some fixed-wing aircraft, post-stall operations are not as atypical as one would believe, and a solid understanding of post-stall aerodynamics is crucial to the success of such applications.

In addition to these applications, post-stall conditions are often encountered in "Loss of Control (LOC)" scenarios. These are defined as "... significant, unintended departure of the

aircraft from controlled flight, the operational envelope, or usual flight attitudes, including ground events" [4]. Given this definition, it is not surprising that the majority of aviation accidents are attributed to LOC situations [5].

A fairly recent example of a LOC accident was the loss of Air France Flight 447 in June 2009 [1]. AF 447 departed Galeo International Airport in Brazil on May 31st, 2009, headed for Charles de Gaulle International Airport in France. At 2:10 am on June 1st, abnormal airspeed indications disengaged the autopilot and auto-thrust systems. It was later found that the abnormal readings were due to icing on the airspeed and angle of attack sensors. The airplane began to roll to the right, and the pilots tried to control the attitude changes by applying a series of high-amplitude roll and nose-up control inputs, causing the aircraft to climb and enter a high-altitude stall, with the angle of attack exceeding the stall angle of 16°. Not recognizing the indications of stall, the pilots continued to make nose-up inputs, and the angle of attack exceeded 40° as the aircraft descended at 10,000 ft/min. The aircraft crashed into the Atlantic Ocean at 2:14 am, killing all passengers and crew.

It is plausible that the pilots flying AF 447 could not recognize the stall due to deficiencies in the aerodynamic models of the flight simulators used to train them [1]. There is a dire need to train pilots in the stall and post-stall regimes so that stall can be recognized and corrected. Increasingly, much of the flight training for airliners is done on flight simulators rather than in a physical aircraft. A significant drawback of this approach is that the lack of reliable post-stall data restricts the accuracy of simulator models.

Efforts have been made in the wind-turbine and helicopter aerodynamics communities to extend airfoil data into the post-stall regime. Models for airfoil force and moment coefficients at high angle of attack conditions have been developed experimentally [6, 7], which has led to researchers proposing empirical models based on flat plate theory [8]. The empirical models developed from experiment require that both the maximum C_l and the corresponding α_{stall} at which this lift coefficient occurs be known reliably before theoretical flat plate data may be fitted to extend the data well into post-stall.

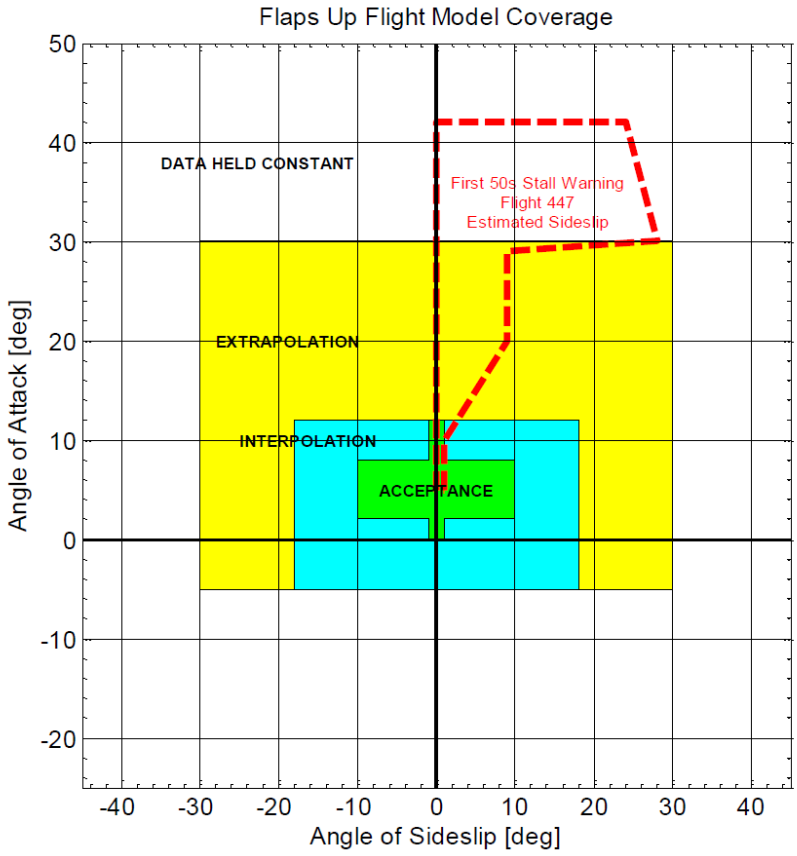

Figure 1.3: Coverage of A330 simulator models, compared to actual AF447 data [1]

Very little data exists in literature covering the stall behavior of finite wings, especially for angles of attack extending deep into post-stall. Published work in post-stall wing aerodynamics often covers general stall behavior, dependent on factors such as planform, without providing detailed force and moment data beyond initial stall [9]. Some studies propose empirical methods based on theory to extend existing force and moment coefficient data-sets deep into post-stall taking into account 3D effects with some correction for aspect ratio [7]. An interesting, purely experimental study, that covers the stall of both a 2D airfoil section and 3D wings of various aspect ratios was performed by Ostowari and Naik [10, 11, 12]. The study presented consistent lift coefficient versus angle of attack data for various NACA 44XX series airfoils and 3D rectangular

wings with a range of aspect ratios having the same airfoils as cross sections.

Research performed under the NASA Aviation Safety Program has had some success in expanding the modeling capability beyond stall for transport-type configurations. Researchers in this program have demonstrated the utility of CFD [13] and experiment [14] in representing the forces and moments at stall and post-stall conditions. While the characteristic behaviors observed in these studies can be modeled and appended to existing models for similar transport configurations, their applicability to other configurations is unknown.

1.2 Suitability of low-order methods

A common method used by modern flight simulation models is to use look-up tables developed from CFD and/or experiment. The state of the art in high-alpha modeling is severely restricted by the lack of reliable data from experiment or CFD. This is partly due to the significant amount of effort and expense required to obtain such data. Attempts to model the post-stall region in simulators generally involve extrapolation or, if possible, interpolation of data outside of the range of coverage. However, comparisons between these models and data obtained from real LOC incidents show a substantial difference [15] that must be diminished to improve flight simulation models so that pilots are better prepared to handle situations involving high angles of attack.

Another method, seen in commercial desktop flight simulators like X-Plane [16] and FS One [17], is to use strip-theory and a component buildup approach. Strip theory posits that the lifting surface can be discretized into "strips", and the forces and moment on each strip are a result of the flow over every strip. These forces and moments are then integrated to obtain the net force and moment on the body. The component buildup method then calculates the force on the vehicle by adding the forces on each body. However, these use an empirical or semi-empirical approach that relies on data from CFD, wind-tunnel experiments, flight testing results, and analytical predictions. Since these empirical methods must be tailored for different configurations, a physics-based, predictive model is highly desirable.

Aerodynamic models that can be used to rapidly calculate forces and moments acting on the wing of an aircraft have applications in design, simulation, and flight dynamics characterization. Low-order methods are especially suitable for these applications on account of their quick solutions, sometimes even in the loop of real-time simulation environments. Low-order methods like the Vortex Lattice Method (VLM) are well established for predicting forces, moments, and spanwise loading characteristics on wings of various planforms at low angles of attack.

Extensive research has been carried out [18, 19, 20, 21, 22, 23, 24, 25, 26, 27, 28, 29, 30, 31] to extend the VLM and similar low-order methods to high angle of attack flow regimes at and even slightly beyond maximum wing lift. A common approach is to modify the potential flow-based equations of traditional low-order methods to model the effects of thick and separated boundary layers. Often, this modification is achieved using a strip-theory based approach, wherein the wing is discretized into strips and each strip is approximated to an airfoil. For each "airfoil," viscous input data is supplied, often in the form of airfoil lift characteristic (C_l-α) curves which form the convergence criteria while solving the 3-D potential flow equations to calculate spanwise loading. This approach yields sufficiently accurate results [29] for simple unswept geometries, providing a significant cost-benefit compared to higher fidelity approaches such as computational fluid dynamics.

Modeling the lift characteristics of swept wings using this method yields poor results. The geometry of swept wings induces pressure gradients in the spanwise direction, especially at the high-loading conditions encountered at high inflow angles. These spanwise pressure gradients move the boundary layer from the root to the tip on aft-swept. The separated flow encountered at high angles of attack is moved tipwards, causing a non-uniform change in the shape of the effective body across the span. On aft-swept wings, it is observed that the root sections encounter an extended range of attached flow, while the tip sections encounter separation at significantly lower inflow angles than on similar wings without sweep [9]. The change in separation behavior of the sections invalidates the assumption that the airfoil C_l vs. α curve is representative of behavior of the strips.

A method developed at NCSU to model the high-alpha deviation in lift from the potential-flow lift line uses the concept of iterative "decambering" — a reduction in the camber of wing sections to account for the effects of the separated boundary layer — to calculate the lift generated by a wing. This method too, is subject to the shortcomings discussed above since viscous airfoil lift curves are used to characterize the sections.

Motivated by the success of low-order methods in predicting low-alpha wing behavior, and high-alpha wing behavior on unswept wings, further research was initiated to develop corrections to the NCSU Decambering Method in order to extend it to swept wings. Development of these corrections would require detailed study of the flow physics for swept wings at angles of attack starting in the linear region and extending well into stall. Airfoil lift and moment data is readily available in the low-alpha range from a multitude of sources, ranging from experimental data from Abbott and von Doenhoff [32], the University of Stuttgart [33] and University of Illinois at Urbana-Champaign [34, 35, 36], to modern computational approaches to predict sectional aerodynamic characteristics based on arbitrary input geometry, such as XFOIL [37].

A database of post-stall airfoil and wing data, with a similar scope to the Ostowari and Naik study, was desired partly to address this dearth of data in the literature, but primarily to support the effort within the Applied Aerodynamics Group at North Carolina State University to develop the low-order model of post-stall aerodynamics for finite wings via use of existing linear low-order methods (VLM, Weissinger or LLT) corrected for nonlinear sectional airfoil behavior. Details of the development of the low-order method may be found in Ref. [38, 39], with the current status pertaining to its use in real-time simulation of aircraft flight dynamics described in Ref. [40].

1.3 Layout of the thesis

In Chapter 2, an overview of the previous post-stall research at NCSU is presented. This includes the work done towards compiling a database of CFD results [2] ranging from pre-stall well past stall for different airfoil and wing geometries, and the development of a low-order "decambering"

approach [38, 39] to model the drop in lift at high angles of attack, and the shortcomings of the method. Chapter 3 describes the process by which the decambering approach is modified in order to overcome the shortcomings mentioned in Chapter 2. Chapter 4 presents the results for wing lift (C_L) and spanwise lift distribution (C_l vs. y) obtained from the modified decambering method. Finally, the conclusions drawn from the results and recommended future work are discussed in Chapter 5.

Chapter 2

Background

This chapter describes the previous post-stall research at NCSU. Two separate but related projects have been conducted — an effort to develop a low-order model for high-alpha operations [38, 39], and an effort to develop a CFD database of various airfoils and wing configurations from pre-stall to deep-post-stall angles of attack [2, 3]. The solutions from this database are used to validate the low-order method, as well as to study the flow-physics at high angles of attack to aid the further development of the low-order method.

2.1 High-alpha CFD

The NASA Tetrahedral Unstructured Software System (TetrUSS) [41] is a package of loosely integrated software, developed to allow rapid aerodynamic analysis from simple to complex problems. The system has its origins in 1990 at the NASA Langley Research Center and has won the NASA Software of the Year Award twice. TetrUSS has been used on high priority NASA programs such as Constellation and the new Space Launch System for aerodynamic database generation along with work in the Aviation Safety Program.

2.1.1 CFD database generation

The component software packages are assembled such that a user follows a systematic process during each application of TetrUSS. There are software packages for preparing geometries for grid generation (GridTool), generating unstructured surface and volume grids (VGRID) and calculating flow solutions (USM3D). Post-processing the solutions with TetrUSS can be done using the included SimpleView software or by easily converting for use with other commercial packages (eg Tecplot, EnSight etc.).

For preparing geometries for grid generation, GridTool is used to generate the necessary VGRID [42] input files. GridTool can read Non-uniform Rational B-Spline (NURBS) curves and surfaces through an Initial Graphics Exchange Specification (IGES) file, as well as PLOT3D point cloud surface definitions. In the database generated by Petrilli [2], geometries were generated using Open Vehicle Sketch Pad (OpenVSP) [43], and converted to the IGES format using Rhino 3D. A flow chart showing the process of geometry generation can be seen in Figure 2.1

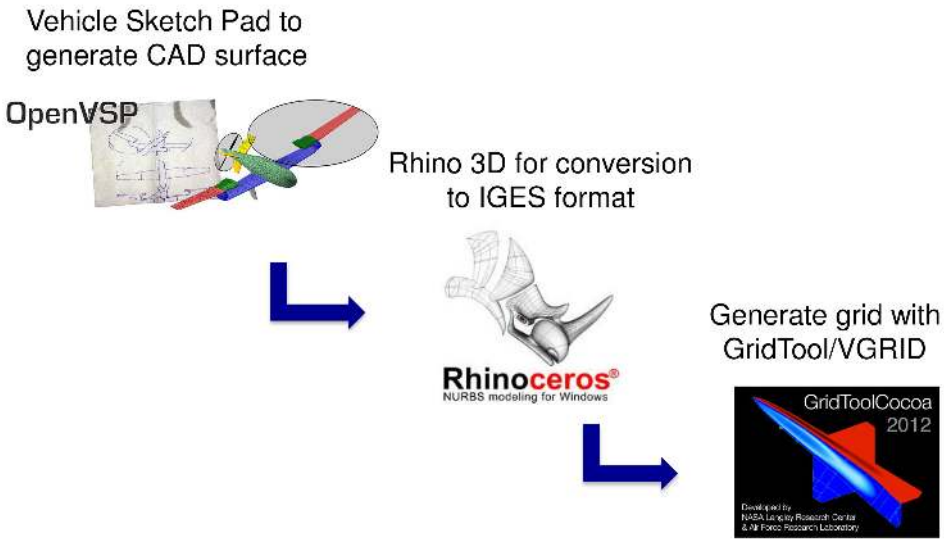

Figure 2.1: Geometry generation using OpenVSP

VGRID is the unstructured grid generation tool used in the TetrUSS Package. Viscous layer generation is accomplished via the Advancing Layers Method (ALM) [44]. Tetrahedral cells are generated in an orderly manner, "marching" nodes away from the surface. After the viscous layers are generated, VGRID then utilizes the Advancing Front Method (AFM) [45] for the generation of the inviscid portion of the volume grid. VGRID can not always close the grid completely. When this occurs, a slower but more robust auxiliary code called POSTGRID is used to complete the formation of the remaining tetrahedral cells.

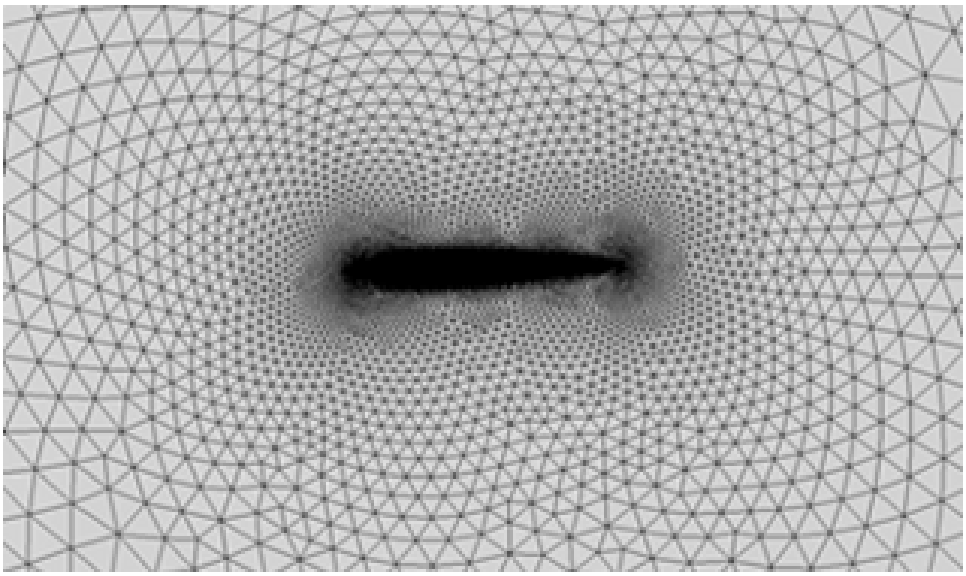

Figure 2.2: The grid generated using GridTool for the NACA 0012 airfoil

For airfoil calculations, a quasi 2D grid was generated on a constant-chord, short-span wing, between two reflection plane boundary condition patches. Figure 2.2 shows a completed grid for an NACA 0012 airfoil. A general goal was set to maintain very similar grid density between the 3D wing grids and the airfoil grids. This is necessary because the airfoil results were being used as input data into the low-order method discussed in the introduction while the 3D wing results from USM3D were being used to assess the accuracy of the low-order method

The flow solver at the core of the TetrUSS package is USM3D [46]. USM3D is a parallelized,

tetrahedral cell-centered, finite volume Reynolds Averaged Navier-Stokes (RANS) flow solver. It computes the finite volume solution at the centroid of each tetrahedral cell and utilizes several upwind schemes to compute inviscid flux quantities across tetrahedral faces. USM3D has numerous turbulence models implemented for use; The simulations assumed the flow to be completely turbulent, and the Spalart-Allmaras (SA) one-equation model [47] was used as the turbulence model in the results used in this study.

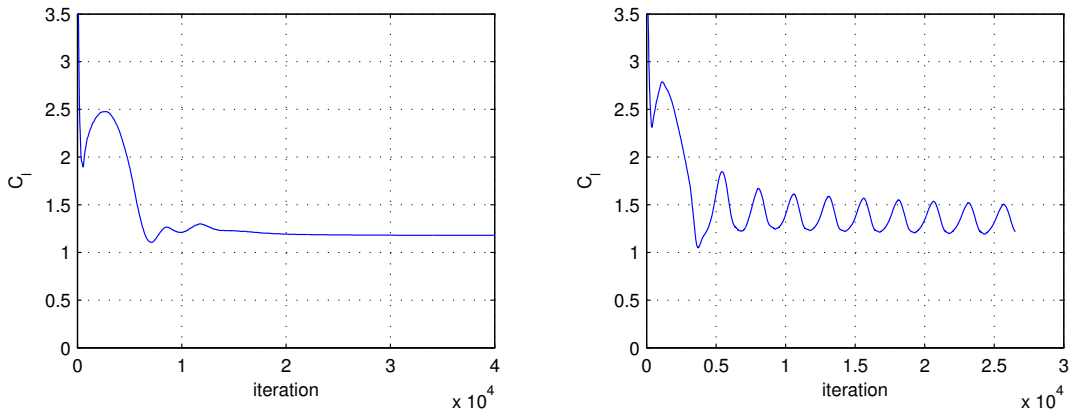

(a) Smooth convergence

(b) Oscillatory convergence

Figure 2.3: Two convergence plots for the NACA4415 airfoil at (a) $\alpha = 30°$ and (b) $\alpha = 48°$ [2, 3].

Convergence of key quantities, like lift, were monitored at each iteration to make sure the solution had converged [2, 3]. Some cases displayed unsteady behavior with oscillatory convergence, seen in Figure 2.3. Refs. [2, 3] describe the monitoring of convergence in detail.

2.1.2 CFD validation

The 2-D RANS CFD results were compared with experimental results generated by Naik and Ostowari in the Texas A&M University Low-Speed Wind Tunnel Facility [10, 11]. In contrast to most available aerodynamic data sources, where data is presented for either an airfoil or a finite wing, the study by Naik and Ostowari presents data for the NACA 4415 airfoil and wings using

NACA 4415 having various aspect ratios. Further, this data set covers a more broad range of α values than is typically available in the literature.

Figure 2.4a presents computational results for C_l, C_d, and C_m vs. α for the NACA 4415 airfoil at $Re = 1$ million and 3 million. Digitized data from the Naik-Ostowari study at the same flow conditions are co-plotted for comparison. Typically, RANS methods are not recommended for high-α (highly separated) flows. A more advanced computational method, Detached Eddy Simulation (DES), is normally used, with an order of magnitude increased expense. However, a comparison between the URANS analysis and experiment shows that, while the two do not match exactly, good agreement exists between them.

Addressing the lift behavior first, both CFD and experimental data show a nearly linear relationship between C_l and α at low angles of attack. However, there is a noticeable difference in $dC_l/d\alpha$, α_{0L}, and the $C_{l,max}$ between the CFD and experimental results. The authors of Reference [10] indicate that the experimental data exhibits a lift curve slope of 0.09 per degree in the low-α range, less than 0.11 measured in Reference [32] and as predicted by thin airfoil theory aerodynamics [48]. Naik and Ostowari attribute the discrepancies in lift-curve slope to bending and twisting of the wind-tunnel model, paticularly as the model is loaded at higher angles of attack. In contrast, the CFD results show the expected lift-curve slope of 0.11 per degree in the low-α range.

The α_{0L} offset motivated additional study; an XFOIL [37] solution using the exact airfoil coordinates run in the CFD was generated at a $Re = 1$ million with the flow tripped at $0.02c$ on the upper surface and $0.1c$ on the lower surface. The α_{0L} value from CFD and XFOIL are nearly indistinguishable. This provides confidence that the CFD correctly predicts the low-α lift characteristics of the airfoil.

Figure 2.4b compares the results for C_L and C_D vs. α for a rectangular wing having the NACA 4415 airfoil and $\mathcal{AR} = 12$. Again, the difference between the CFD and experimental results in α_{0L}, $dC_L/d\alpha$ and $C_{L,max}$ can be attributed to errors in the experimental setup due to a non-rigid wing model.

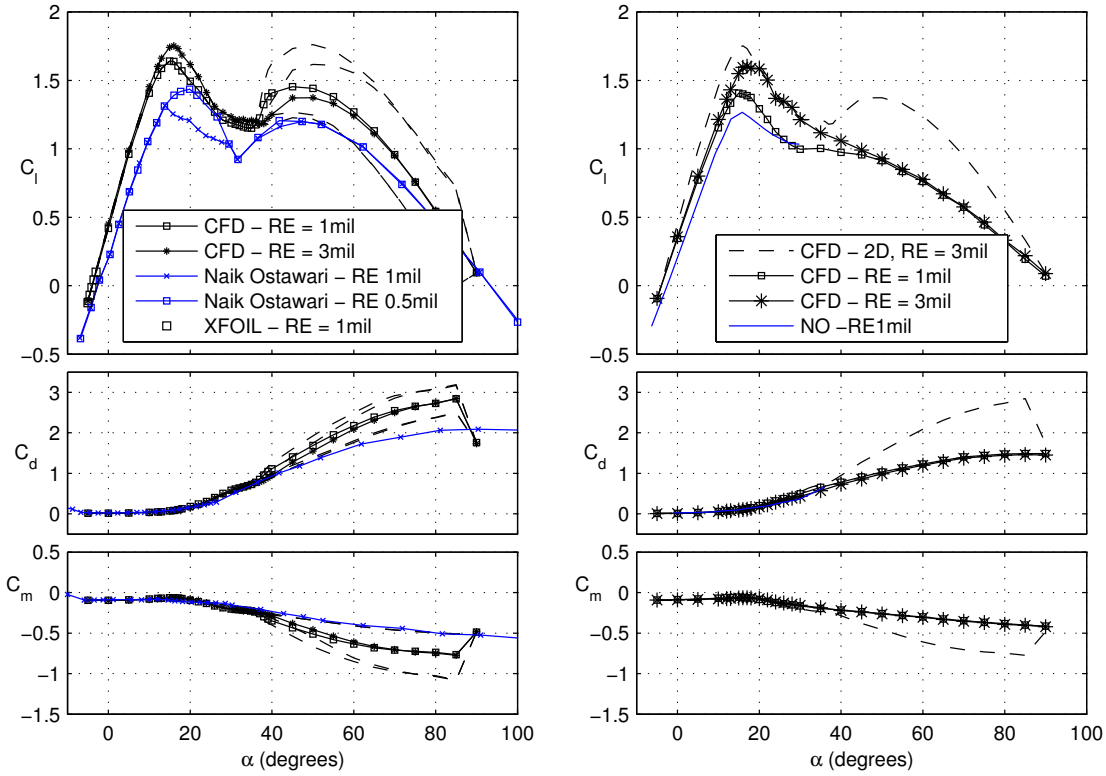

(a) (b)

Figure 2.4: Lift, drag, and moment polars from CFD and experimental data for (a) the airfoil, and (b) the unswept wing

2.2 Modeling post-stall aerodynamics using the NCSU decambering method

The Applied Aerodynamics Lab at North Carolina State University has been developing a rapid, low-order wing stall prediction method [38, 49] since 2002. This method uses the concept of viscous decambering at large angles of attack to simulate the effects of the separated boundary layer. Decambering can be applied to an inviscid low-order method such as lifting-line theory, Weissinger's method, or the vortex lattice method to extend it beyond the linear region into the stall and post-stall regimes.

2.2.1 Illustration of the decambering concept

The concept of decambering is best explained using the simple example of two-dimensional flow past an airfoil. This approach is then extended to the flow past a 3-D wing.

At low angles of attack, the flow past the airfoil behaves like inviscid flow, and is fully attached to the surface of the airfoil. With an increase in the angle of attack, the boundary layer on the upper surface begins to separate, and at some angle of attack, is fully separated from the airfoil. The thickened boundary layer changes the effective shape of the airfoil, reducing its effective camber. This camber reduction, or "decambering" results in a reduced circulation, and causes the deviation from the inviscid lift curve predicted by thin airfoil theory. The current decambering approach developed at NCSU is based on the idea that the potential-flow prediction of C_l for the decambered airfoil will match the viscous C_l of the original airfoil, even if the angle of attack is well beyond the stall angle. The decambering can be modeled as an effective reduction in the chordwise distribution of camber using a decambering variable, $\delta_1 = (C_{l,\text{viscous}} - C_{l,\text{inviscid}})/2\pi$.

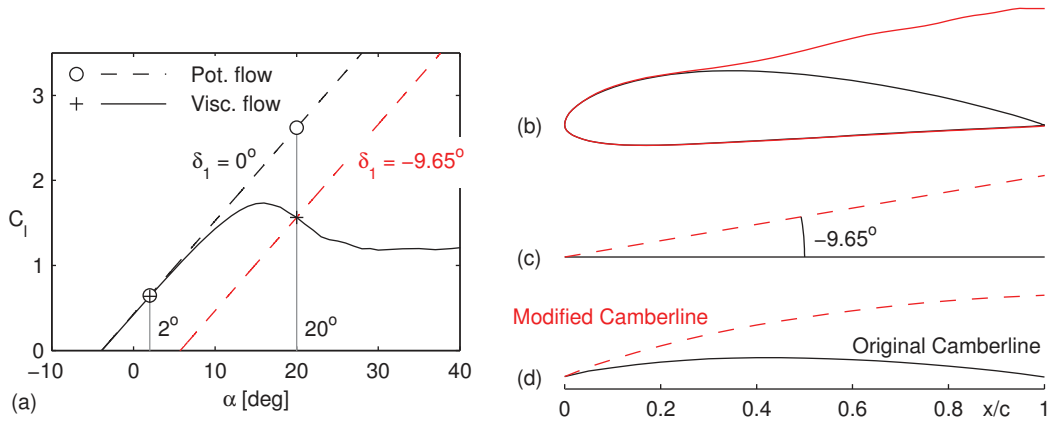

Figure 2.5: Illustration of decambering for an airfoil: (a) Potential flow and viscous flow lift curves and operating points for an airfoil at low and high α; Potential-flow curves are shown for $\delta_1 = 0°$ and $-9.65°$, (b) airfoil geometry with boundary-layer displacement thickness at high α, (c) equivalent decambering using single-variable decambering, and (d) original and modified camberlines.

Figure 2.5 illustrates the concept when applied to an airfoil. Figure 2.5(a) compares the lift curves obtained from potential-flow and viscous solutions. At low angles of attack, it can be seen that the C_l values predicted by both methods are nearly identical. At high angles of attack, in this example 20°, the C_l obtained from the potential flow solution differs significantly from that given by the viscous solution. Figure 2.5(b) shows the flow separation that causes this difference in lift. This flow separation is modeled as a reduction of camber, as seen in Figure 2.5(c), which when added to the original camberline, gives a modified camberline for the effective airfoil body as shown in Figure 2.5(d). Figure 2.5(a) also shows the potential-flow solution for the modified airfoil with $\delta_1 = -9.65°$. This matches the viscous solution at $\alpha = 20°$, confirming that $\delta_1 = -9.65°$ is the appropriate amount of decambering for this airfoil at this angle of attack.

2.2.2 Post-stall aerodynamics of finite wings using iterative decambering

At high angles of attack, the boundary layer thickens and later separates, which causes the deviation of viscous C_l from inviscid predictions. This behavior can be modeled in a potential flow method by a change in the chordwise distribution of camber. A potential flow method can then be used to predict the lift on the modified airfoil. Further research has shown that this method can reliably be used for lift calculations on rectangular and slightly swept wings. [39, 50, 51]

The VLM is an efficient computational tool to solve the 3-D potential flow problem, and is described in detail by Katz and Plotkin [48]. The implementation used here is a variation of the VLM formulated by Murua et al [52]. In the VLM, elementary solutions (vortex-rings) are distributed over mean camber line of the wing surface. The leading segment of the vortex ring lies on the panel's quarter-chord line, and a collocation point is placed at the three-quarter-chord line, which falls at the center of the vortex ring. In the current implementation, a steady wake model is assumed; this wake is assumed to be flat (no roll-up model used), and is carried downstream to infinity. Figure 2.6 shows the panel discretization for an example 30 degree sweep

wing, and shows the bound and wake vortex rings for a given strip, j.

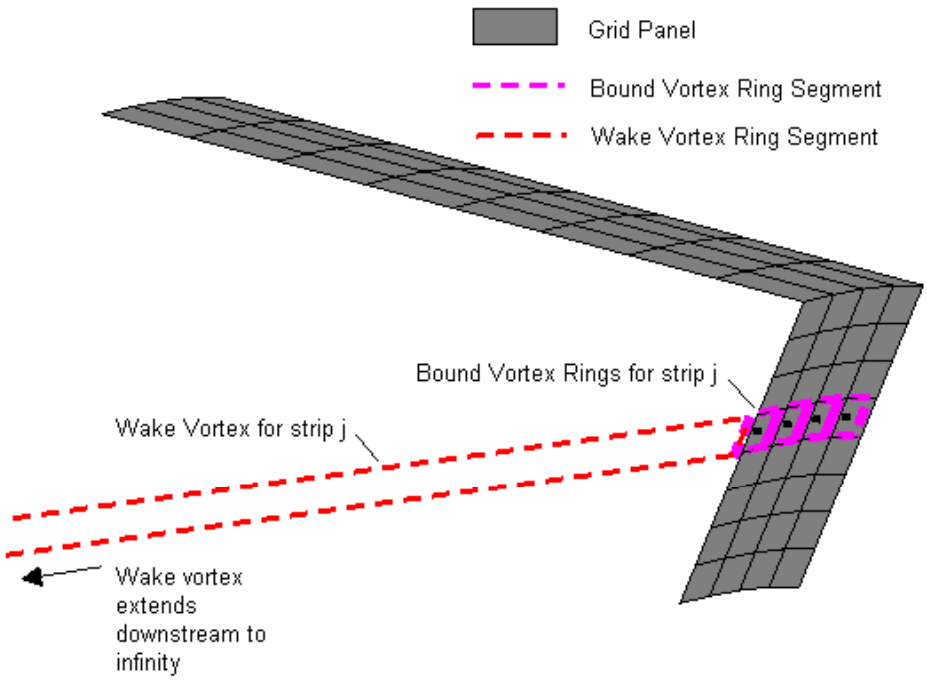

Figure 2.6: Steady aerodynamics model: lifting-surface and wake discretization using vortex-ring elements.

Along with the discretization of the geometry and placement of vortex rings, each strip is assigned a viscous C_l-α curve as part of input data. This data is used as convergence criterion for the decambering approach, which calculates a decambering variable, $\delta(j)$, for each strip j. The decambering variable is essentially a rotation of strip normal vectors. In past implementations of the decambering approach, the input C_l-α information was the lift curve data for the corresponding airfoil section. This approach worked well for unswept wings, but resulted in poor stall predictions for aft-swept wings for which spanwise pressure gradients result in tipward transport of separated boundary layer. As described later in this paper, the current work explores the use of modified C_l-α information for the sections to improve predictions of

stall characteristics on swept wings.

Using the fixed aerodynamic geometry (Figure 2.6), the non-penetration boundary condition is applied to each collocation point to obtain a system of algebraic equations. The vorticity distribution is determined by

$$[AIC]\,\boldsymbol{\Gamma} + \boldsymbol{w} + \boldsymbol{w_{dec}} = 0, \tag{2.1}$$

where $\boldsymbol{\Gamma}$ is a column vector with the circulation strengths of the bound vortex rings. It is worth noting, that for a steady wake, the circulation strength in the wake vortex ring corresponding to spanwise location j is equal to the circulation strength in the trailing edge chordwise panel at station j. AIC is the aerodynamic influence coefficient matrix, computed at the collocation points using the Biot-Savart law, and accounts for induced velocities caused by both bound and wake vortices. $\boldsymbol{w}$ in Equation (2.1) is the column vector of normal components of all velocities except those induced by bound and wake vorticity, which may encompass deployment of control surfaces, gust-induced velocities, and rigid-body motions, and will be denoted here as "non-circulatory velocity". $\boldsymbol{w_{dec}}$ in Eq. (2.1) is the column vector of normal components of velocity due to decambering, which is modeled as by tilting the normal vectors of a strip by a decambering angle δ.

Aerodynamic analysis for an inflow condition begins by assuming $\boldsymbol{\delta} = 0$. The circulation strengths are solved for using Equation (2.1), and converted to aerodynamic forces through the Joukowski theorem:

$$\vec{F}_{inv} = \rho \vec{V}_{\text{inf}} \times \vec{\Gamma}_b \tag{2.2}$$

Next, local aerodynamic coefficients and angle of attack are computed for each section using Equations (2.3) and (2.4).

$$C_{l_{sec}}(j) = \frac{|\vec{F}_{cl}(j)|}{1/2\rho|\vec{V}_{\inf}|^2 dS_{strip}(j)} \tag{2.3}$$

$$\alpha_{eff} = (C_l)_{sec}/a_0 - \delta - \alpha_{0l} \tag{2.4}$$

If the computed points $(\alpha_{eff}(j), C_{l_{sec}}(j))$ fall upon the input viscous data for section j, as they will for a pre-stall case, no decambering is necessary. If this convergence criteria is not satisfied, decambering is applied according to:

$$\delta^{new}(j) = \delta^{old}(j) - \frac{\Delta C_l}{\frac{\partial C_l}{\partial \delta}} \tag{2.5}$$

The numerator term in Equation (2.5) represents the error in C_l (the residual) for a given strip. The denominator represents the change in decambering required to elicit a desired change in operating C_l for a given strip. Details for these terms are provided in Reference [39]. If the residual is greater than the predefined tolerance, each element of the $\boldsymbol{\delta}$ vector is altered according to Equation (2.5) and the aerodynamics are re-evaluated until the operating points are converged on the viscous input data. The total wing C_L is not evaluated until the circulation strengths computed using the modified vortex lattice satisfy both the boundary-condition equation (Equation (2.1)) and the sectional C_l values all fall on their respective input data.

2.2.3 Iterative decambering applied to swept wings

As suggested before, there is flow in the spanwise direction on the wing due to the pressure gradients created because of the wing sweep. Figure 2.7 demonstrates this behavior by showing surface skin-friction lines on wings with sweep from 0° to 30° . Note that the amount of spanwise flow increases with increasing sweep. The resulting spanwise transport of the separated boundary layer at high angles of attack changes the sectional behavior.

Applying the decambering method, as described in Section 2.2.2 using readily available

airfoil sectional input data is expected to fail when applied to swept wing cases. Figure 2.8 demonstrates this expectation, as the low-order aerodynamic prediction is shown to predict the maximum wing C_L quite well for the rectangular wing, but becomes progressively worse as sweep is applied.

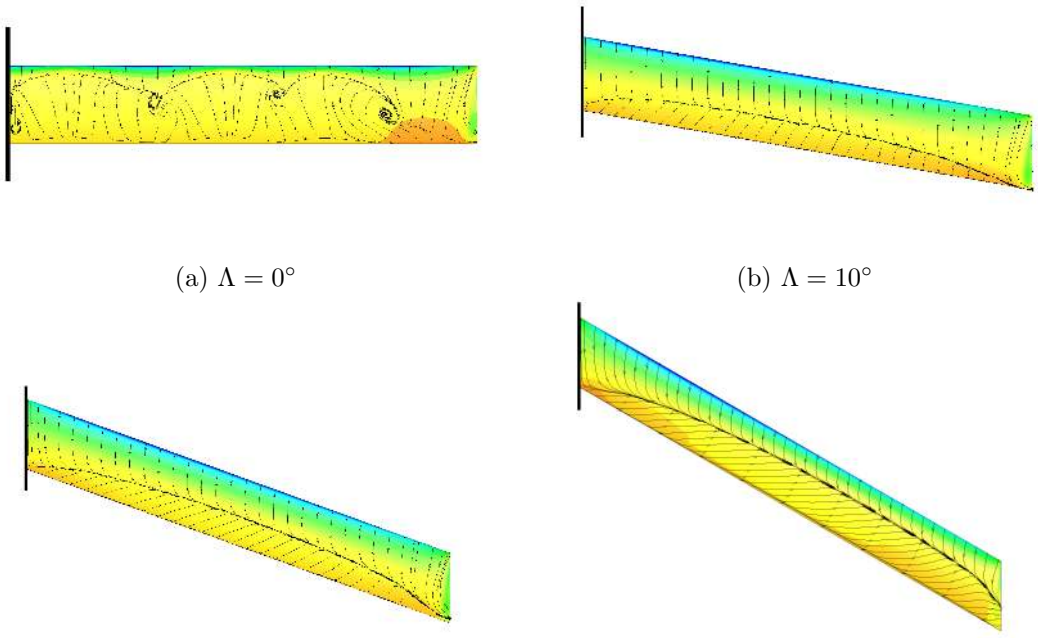

(a) $\Lambda = 0°$ (b) $\Lambda = 10°$

(c) $\Lambda = 20°$ (d) $\Lambda = 30°$

Figure 2.7: Streamlines at $C_{L,max}$ for $\mathcal{AR} = 12$ wings with sweep angles 0°, 10°, 20°, and 30°.

Use of the airfoil lift curves in application of the decambering approach to swept wings clearly results in poor prediction of stall characteristics. The research presented in this thesis aims to explore the use of modified airfoil lift curves derived from the study of RANS computational results, generated using the TetrUSS CFD software package, in conjunction with the iterative decambering approach to study whether the strip-theory based methods remain applicable for swept wing stall prediction.

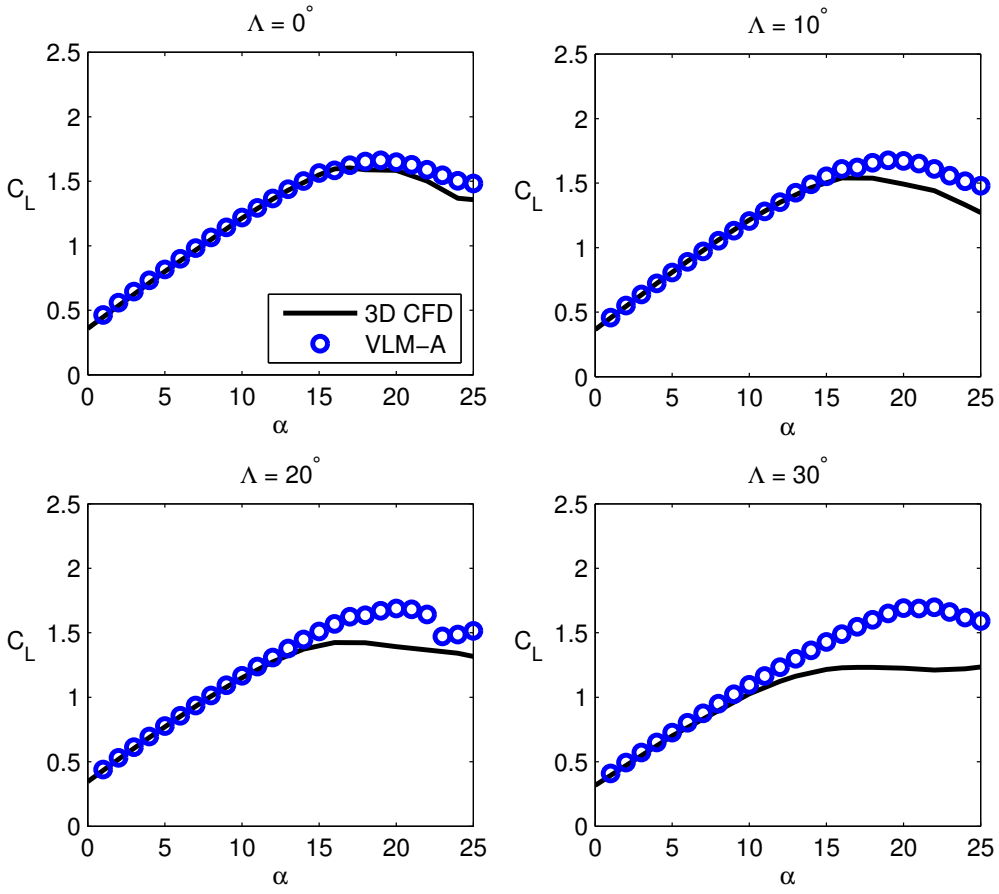

Figure 2.8: VLM with decambering, using viscous airfoil input data (VLM - A), applied to wings with sweep angles of 0°, 10°, 20°, and 30°.

Chapter 3

Modifications to Iterative Decambering to Account for Spanwise Boundary Layer Transport

In order to account for the effects of boundary layer thickness at high angles of attack and the resulting spanwise transport of the boundary layer on wings with sweep, the VLM requires the section lift characteristics at multiple stations across the span. The database of CFD results described in Chapter 2.1 is used to obtain the input data required by the decambering method. Four constant-chord wings with the NACA 4415 airfoil and $\mathcal{AR} = 12$ are considered, with sweep angles of 0°, 10°, 20°, and 30 degrees. Pressure and friction coefficients are extracted at multiple spanwise locations across the surface of the wing. This data is then used to calculate the forces on the section. Another important parameter extracted from the CFD database is the location of the trailing-edge separation point, f. These parameters are then used to determine the local operating angle of attack. Certain trends observed in the variation of the location of the separation point with spanwise location and operating α. These trends can then be used to calculate the true operating lift characteristics of the sections. The true lift curves are now used as input to the decambering method. Figure 3.1 shows an overview of the method, described in

detail in the following sections.

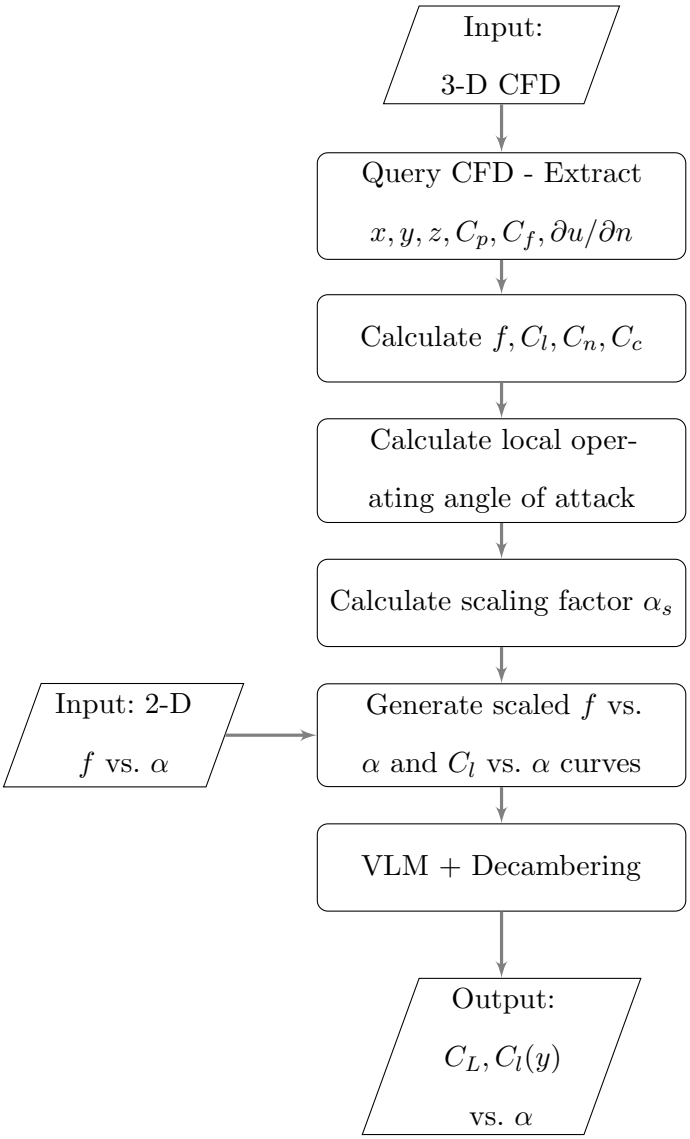

Figure 3.1: Flowchart for the method.

3.1 Extraction of data from the CFD solutions

The flow properties used to calculate the necessary modifications to the decambering method are extracted from the CFD database described in Section 2.1. All CFD cases in the database follow the axis convention shown in Figure 3.2: the chord is aligned with the X direction, and the span is aligned with the Y direction.

The airfoil CFD case uses a quasi-2D grid, with a constant-chord airfoil section and reflection planes at both ends. Since the flow properties at all sections are the same, the airfoil data is extracted from a single XZ plane at the mid-span point using Tecplot 360. A screenshot of the slice at which data is extracted is shown in Figure 3.2

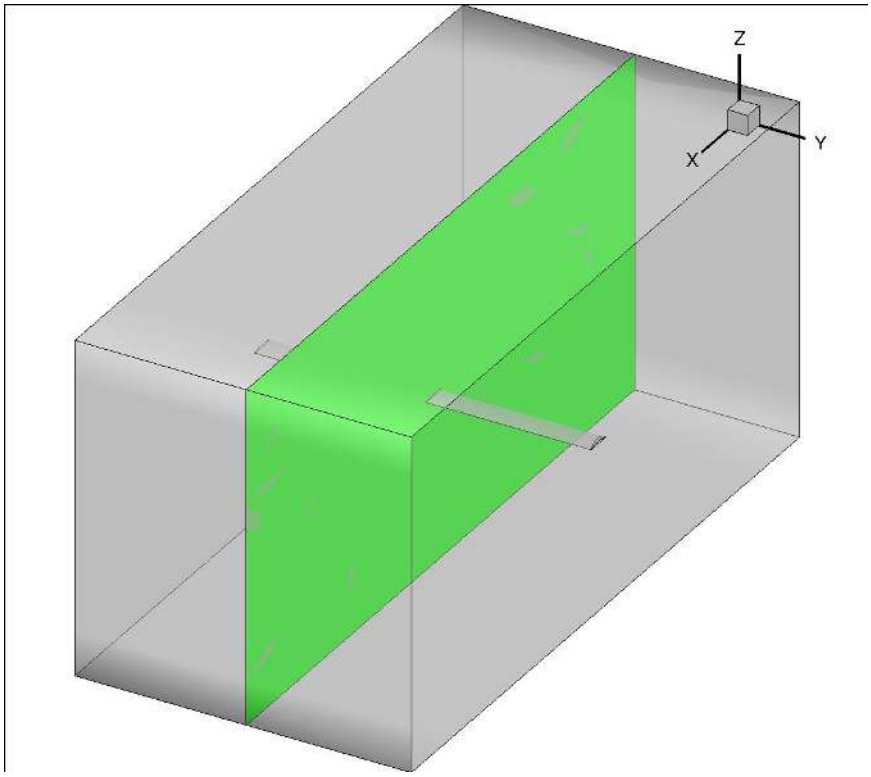

Figure 3.2: Flow properties at an XZ plane being extracted using Tecplot 360. The axis convention used is shown in the upper right.

The wing CFD results are all half-span geometries with a reflection plane at the wing root. Since the flow over the wings is not two-dimensional, data from the wing cases was extracted at multiple, evenly placed spanwise planes, shown in Figure 3.3.

The process was automated by MATLAB and shell scripts to create and run Tecplot macros that would extract the flow properties at all the required sections. The extracted data was then processed in MATLAB to obtain the C_l, C_n, C_c, and f at each section.

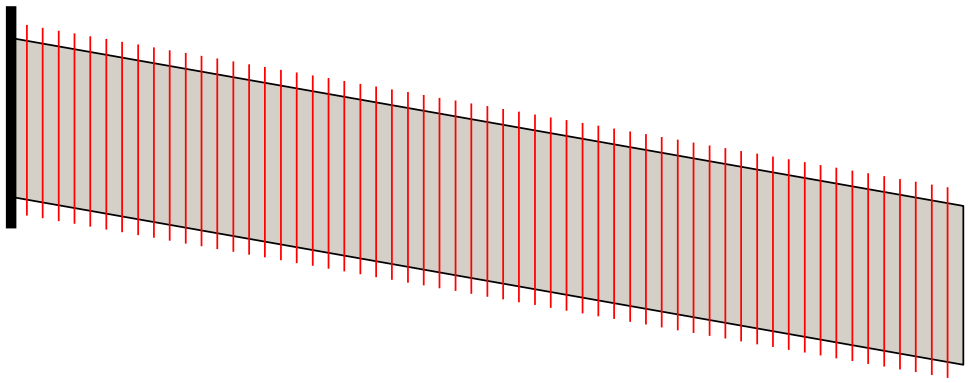

Figure 3.3: The wing planform with sweep angle $\Lambda = 10°$. The red lines denote the sections where data was extracted.

3.2 Force calculation

Figure 3.4 shows the forces acting on each section. The free stream, as seen by the section, has a velocity V_∞, and is at an angle α with respect to the chord- line. The normal force, F_n acts perpendicular to the chord-line, and the chordwise force F_c acts along the chord-line. The sum of these forces, F_{net}, is resolved perpendicular and parallel to the direction of the freestream velocity vector to obtain the lift and drag forces, F_{lift} and F_{drag}. Each force, divided by the dynamic pressure q_∞, gives the corresponding coefficient.

The lift on each wing section is the vector sum of the pressure and friction forces acting on each panel.

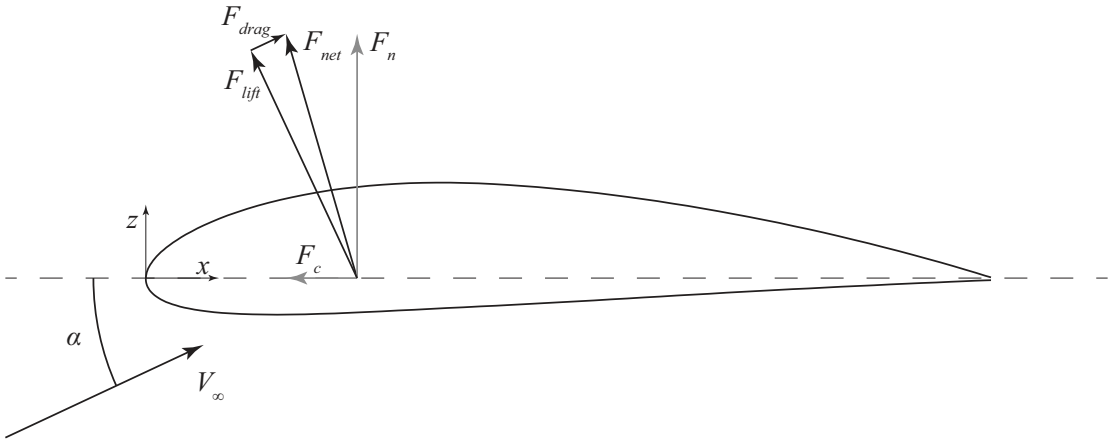

Figure 3.4: Forces acting on the wing section

$$\frac{\vec{F}_{net}}{q_\infty} = \frac{1}{c}\sum\left[C_p\ \left(\vec{\delta l}\times\vec{e}_y\right) + C_f\ \vec{\delta l}\right]$$
$$C_x = \frac{\vec{F}_{net}}{q_\infty}\cdot\vec{e}_x$$
$$C_z = \frac{\vec{F}_{net}}{q_\infty}\cdot\vec{e}_z$$
$$C_l = C_z\ \cos(\alpha) - C_x\ \sin(\alpha) \tag{3.1}$$

C_x and C_z denote the force coefficients in the chordwise and normal direction respectively.

3.3 Location of the flow separation point on the upper surface

For the airfoils of interest in this work, stall is preceded by the boundary layer separation gradually progressing upstream from the trailing edge with an increase in the angle of attack. The location of the separation point is critical to the method since it is required to calculate the operating angle of attack for the wing sections, described in Section 3.4. The separation point can be found by locating the point on the airfoil at which the surface shear force is zero while changing direction from positive to negative.

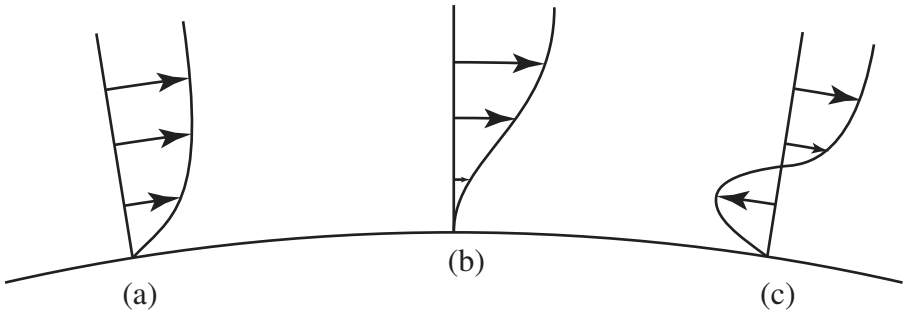

Figure 3.5: Flow in the boundary layer: (a) before, (b) at, and (c) after separation.

The shear stress at any point on the airfoil can be found from Newton's law of viscosity, calculated at the airfoil wall, where n is the distance from the surface in the normal direction, and u is the flow velocity parallel to the surface. The shear force, F_{shear} is the surface area, S, times the shear stress.

$$\begin{aligned} \tau_{wall} &= \mu \left.\frac{\partial u}{\partial n}\right|_{wall} \\ F_{shear} &= S \cdot \mu \left.\frac{\partial u}{\partial n}\right|_{wall} \end{aligned} \tag{3.2}$$

Since μ is constant, and the area is always positive, it is sufficient to monitor the value of $\partial u/\partial n$ to locate the separation point.

Normal vectors to the airfoil are calculated at each point using the coordinates from previously extracted data. The surface of the airfoil at a grid point is taken as the line joining the previous and next points. The normal at a point is the normal to this surface line.

$$\vec{s}_i = \vec{p}_{i+1} - \vec{p}_{i-1} \tag{3.3}$$

$$\vec{n}_i = \begin{bmatrix} 0 & 1 \\ -1 & 0 \end{bmatrix} (\vec{p}_{i+1} - \vec{p}_{i-1}) \tag{3.4}$$

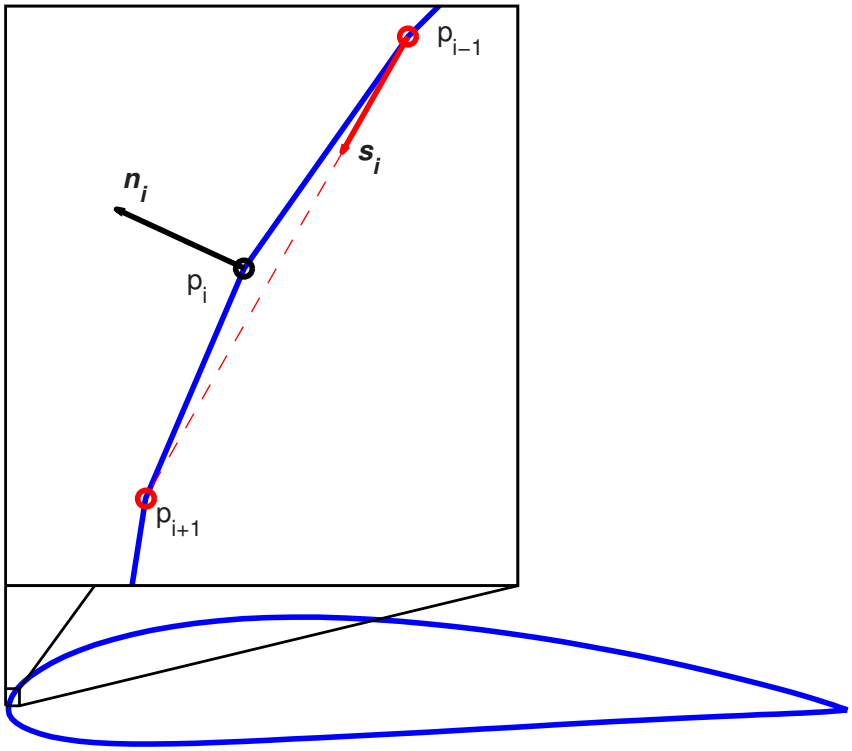

Figure 3.6: Surface and normal vectors

Here, $\vec{s}_i$, $\vec{n}_i$, and $\vec{p}_i$ denote the surface vector, normal vector, and position vector respectively for the i^{th} point of the airfoil. Figure 3.6 shows the surface and normal vectors at a point p_i. Tecplot 360 is used to extract the velocities at two points very close to the surface along the normal vector calculated from Equation (3.4). These velocities are resolved along the surface, and the value of the derivative is calculated using Equation (3.5).

$$\left.\frac{\partial u}{\partial n}\right|_{wall,\ i} = \left(\vec{V}(\vec{p}_i + 2\epsilon\ \vec{n}_i) - \vec{V}(\vec{p}_i + \epsilon\ \vec{n}_i)\right) \cdot \vec{s}_i \tag{3.5}$$

The non-dimensionalized separation location, f, is the value of x/c at the point where $\partial u/\partial n$ flips sign. An example is shown in Figure 3.7, where $f = 0.71$. The streamlines confirm that that this approach yields the correct location of the separation point.

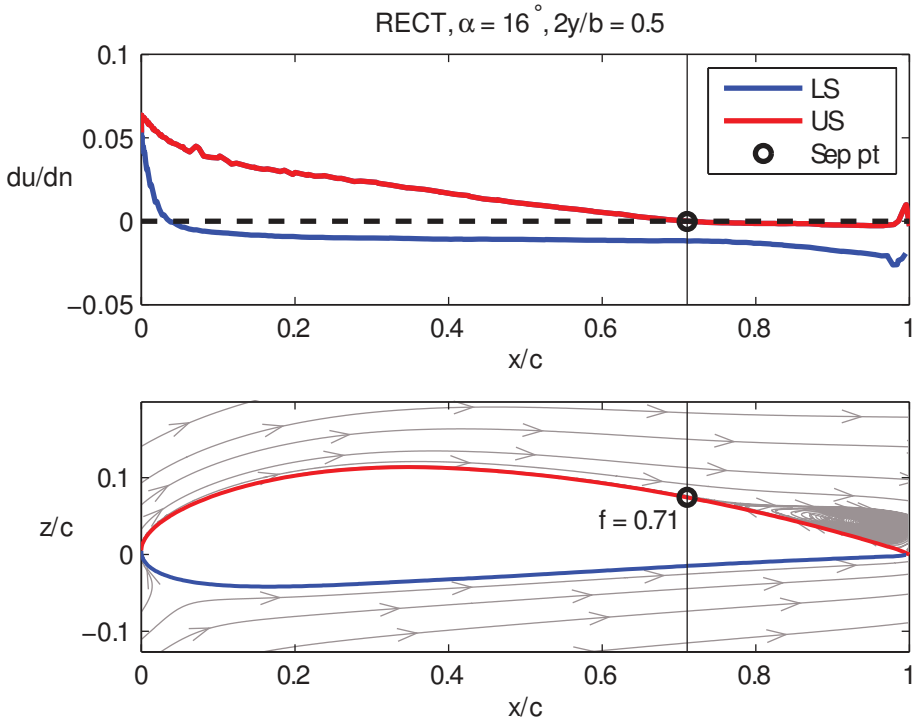

Figure 3.7: Location of the separation point

3.4 Calculation of the operating angle of attack

As discussed previously, the effects of viscosity cause a deviation of the viscous lift curve from the potential-flow lift curve. This deviation occurs as a result of increasing adverse pressure gradients at high angles of attack, which cause the separation of the boundary layer from the wing. The separated boundary layer changes the effective shape of the wing sections, and the resultant lift generated is affected. As a result of this separation and the effects of the induced downwash, the sections operate at angles of attack not necessarily equal to the wing angle of attack. It is necessary to consider this actual operating α instead of the wing α while calculating the section characteristics for input to the VLM.

Flow over rectangular wings is relatively uniform across the span, and most sections encounter similar flow patterns, with the exception of stall cells — regions of separated flow appearing at periodic intervals across the span, with narrow regions of attached flow between cells — that are

formed at high angles of attack [53, 54]. As a result, the characteristics of a single section can be applied to other sections in a method using a strip-theory approach. On the other hand, flow over swept wings is not uniform, due to the spanwise propagation of the separated boundary layer, and each section does not encounter similar amounts of separation. As a result, the operating angle of attack for each section is not necessarily the same.

Beddoes and Leishman [55] developed a model for calculating the lift over an airfoil having separation. This method, based on the Kirchhoff-Helmholtz flat-plate model, gives equations for the normal and chordwise forces encountered by the airfoil as a function of the angle of attack, α, and the non-dimensionalized chordwise location of the separation point, f. The value of f varies from 0 at the leading edge, signifying fully separated flow, to 1 at the trailing edge, signifying fully attached flow. The normal and chordwise force coefficients on the section are given by:

$$C_n = 2\pi \left(\frac{1 + \sqrt{f}}{2} \right)^2 \sin(\alpha) \tag{3.6}$$

$$C_c = 2\pi \sin^2(\alpha) \sqrt{f} \tag{3.7}$$

The 2π in Equations (3.6) – (3.7) denote the potential-flow lift curve slope for an airfoil. This can be replaced by a_0, the actual viscous lift curve slope at low α for the airfoil being used at the design Re and M_∞ if additional accuracy is required. Additionally, the angle of attack measured by Beddoes and Leishman was relative to the zero-lift angle of attack, α_{0L}. The equations can then be rewritten as shown below.

$$C_n = a_0 \left(\frac{1+\sqrt{f}}{2} \right)^2 \sin(\alpha - \alpha_{0L}) \tag{3.8}$$

$$C_c = a_0 \sin^2(\alpha - \alpha_{0L}) \sqrt{f} \tag{3.9}$$

This idea can be extended to apply to wing sections. As discussed earlier, wing sections seldom operate at the same effective angle of attack as the wing itself. The local operating angle of attack, α, can be calculated from the local C_n and the location of the separation point using the Beddoes and Leishman model.

$$\alpha = \sin^{-1} \left(\frac{C_n}{a_0} \left(\frac{2}{1+\sqrt{f}} \right)^2 \right) + \alpha_{0L} \tag{3.10}$$

3.5 Modification of airfoil separation curves to obtain section separation curves

Data extracted from the CFD results for each spanwise section of the wing is used to determine the separation point location, as described in Section 3.3, and the operating angle of attack, as described in Section 3.4. We now have data describing the movement of the separation point with the operating angle of attack (f vs. α) for each section. However, the decambering method requires the lift characteristics (C_l vs. α)at multiple sections as input in order to calculate the lift on the wing. It is difficult to quantitatively calculate the differences between the airfoil and section lift curves, since the lift is not bounded and does not monotonically increase or decrease with α. Two variables are required to quantify the change in the lift curve — $C_{l,max}$ and α_{stall}. Trends observed in the separation point curves (f vs. α) mirror the trends observed in the lift curves — delayed separation and hence delayed stall with higher $C_{l,max}$ at the inboard sections

and the opposite effect at the outboard sections. However, the separation point location, f, always lies between 1 (no separation), and 0 (full separation). Moreover, with an increase in α, we know that f must stay the same or decrease, signifying a forward motion of the separation point. This allows the trends to be easily quantified in terms of a single variable, described below.

The separation point location is found to be dependent on the spanwise location (y) and the local angle of attack (α). For the rectangular wing, as expected, the separation curves at all sections are fairly close to the airfoil separation curves. However, with increasing sweep, a pressure gradient is created across the span. This gradient induces a flow in the spanwise direction, transporting the separated boundary layer from root to tip. As a result, separation near the root is delayed, and the flow at the tip separates at lower angles of attack. This results in a fanning out of the separation curves on either side of the 2-D separation curve. This is depicted in Figure 3.8, which shows the separation curves for the four wings close to the root and tip, and at the mid-span section.

Recognizing that all the section separation curves are similar in shape to the separation curve of the airfoil, it was proposed that the airfoil curve could be transformed to approximate the actual section curve. It is seen that the slope of the separation curve, in the region of partial separation, varies with the spanwise location and sweep angle. Another important observation is that the flow starts separating around the same angle of attack, regardless of the spanwise location or sweep angle. Therefore, a transformation equation was proposed wherein the airfoil curve would effectively be scaled about the α where separation starts, such that the approximated separation curve would coincide with the actual separation curve at the α where separation reaches 50% of the chord-length. Equation (3.11) shows the equation used to transform the airfoil curve.

$$\alpha'(y, f) = \alpha_1 + \frac{\alpha_s(y) - \alpha_1}{\alpha_a - \alpha_1} \cdot [\alpha(y, f) - \alpha_1] \tag{3.11}$$

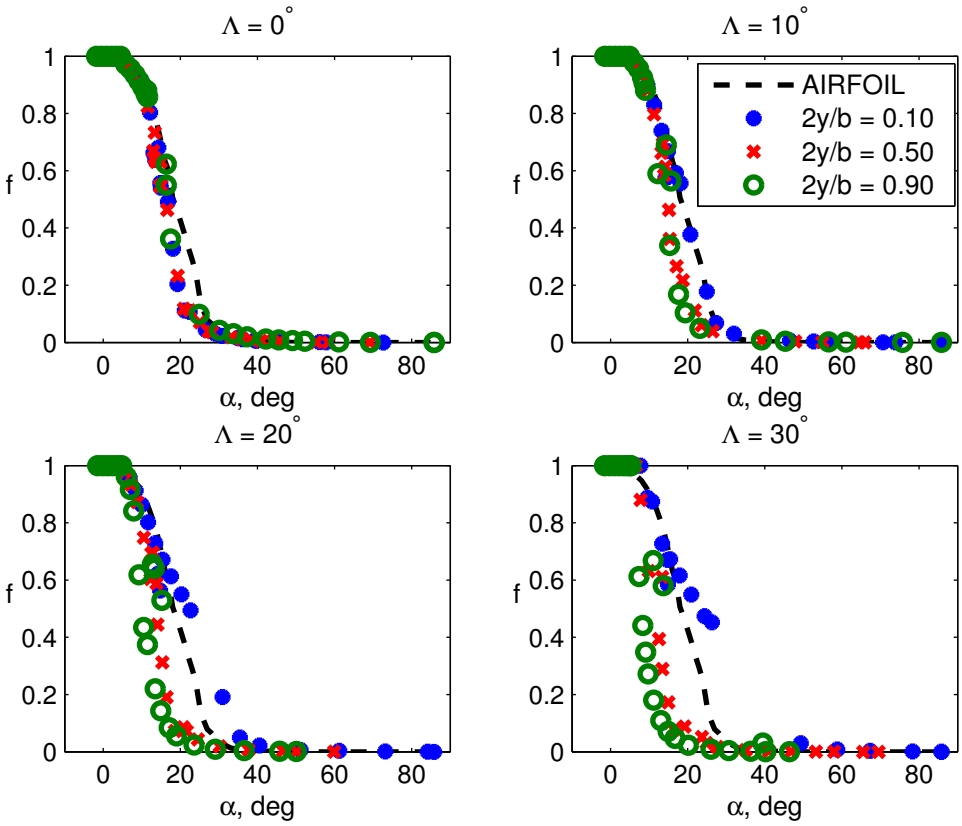

Figure 3.8: Separation curves at the root (10% semispan), mid-span, and tip (90% semispan)

Here, α_s is the local angle of attack at which separation reaches 50% of the chord and depends only on the spanwise location. α_1 is the angle of attack at which the boundary layer on the airfoil just starts separating, and α_a is the angle of attack at which the separation on the airfoil reaches 50%. α_1 and α_a are constant for a given airfoil.

For example, Figure 3.9 shows the approximate and actual separation curves for the 30° swept wing at four spanwise locations from the root to the tip. It is seen that the transformation used to calculate the approximate separation curves yields results that match the actual separation curves reasonably well. Now, knowing the variation of α_s with y for a given sweep angle, and the airfoil properties (airfoil separation curve and α_1), we can predict the section separation curves fairly accurately.

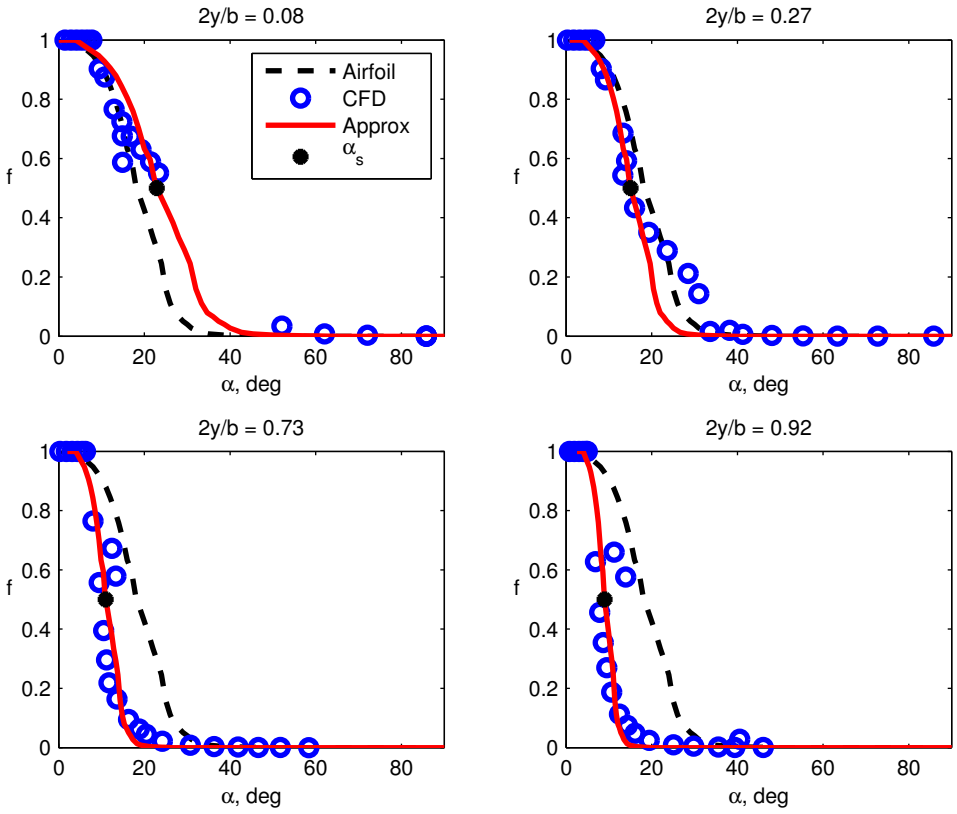

Figure 3.9: Separation curves for the 30° swept wing (CFD) and the approximation generated with Equation (3.11) (Fit).

Figure 3.10 shows the variation in α_s with span and sweep angle. The scaling factor for the rectangular wing varies minimally, and α_s is seen to increase at the root and decrease at the tip. This trend intensifies with an increase in the sweep angle. This is because an increase in the sweep angles causes higher spanwise gradients, and the associated tipward transport of the separated boundary layer exaggerates the change in separation characteristics.

Clear trends were observed in the variation of α_s. It was found that the points could be fitted to a cubic polynomial of the form $\alpha_s(y_{nd}) = a\ y_{nd}^3 + b\ y_{nd}^2 + c\ y_{nd} + d$, where $y_{nd} = 2y/b$, whose coefficients vary with the sweep angle.

These cubic polynomials were then used to look up the value of α_s at any spanwise location.

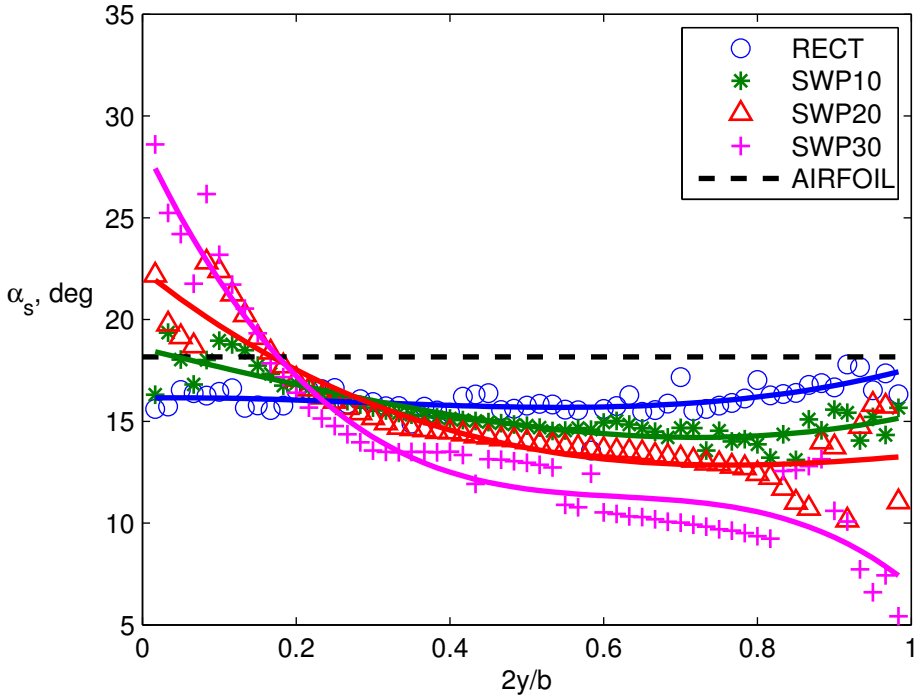

Figure 3.10: The variation of the scaling factor, α_s, with spanwise location and wing sweep (symbols) and the cubic polynomial fit (lines)

This approach eliminates errors seen in an earlier research effort [56] introduced due to irregularities in the flow at certain sections, where α_s is wildly different from that of the surrounding sections. Figure 3.11 shows the variation of the polynomial coefficients with sweep angles. Trends in the variation of the four coefficients with sweep angle can be discerned, which motivates further research to verify if these trends are observed in other airfoil and wing geometries, and if the coefficients for wings having the same airfoil but different sweep angles line up with the trends seen here.

Using the cubic polynomial approximation for α_s, characteristic separation curves can be generated for the wings being studied at multiple spanwise locations. These separation curves are plotted in Figure 3.12. As noted earlier, these curves reflect the actual separation behavior at the different sections of the wings: the plots for the unswept wing show that all sections

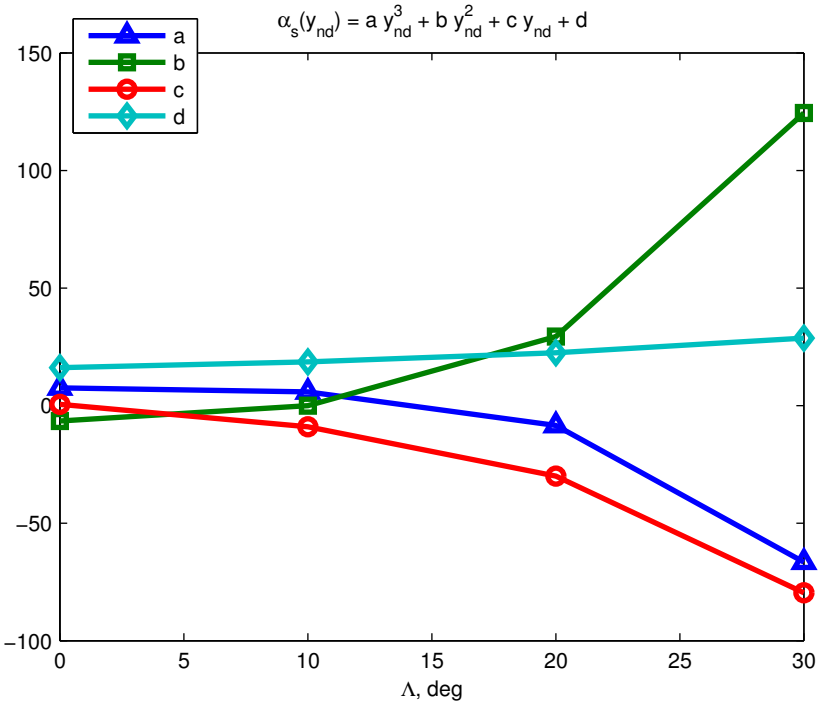

Figure 3.11: Variation of the polynomial coefficients with sweep

behave nearly the same as the airfoil, which is why the original decambering method works so well for rectangular wings. As the sweep is increased, we observe that the separation curves fan out around the airfoil separation curve. This reflects our observation of delayed separation at the inboard sections and premature separation at the outboard sections on account of the spanwise boundary layer transport.

3.6 Generation of the lift curves

The change in the separation characteristics of the sections manifests in the lift characteristics as a delay or advancement in stall. Since the decambering method calculates the values of the decambering variables at the sections as a function of the inviscid C_l and viscous C_l, the separation curves described in Section 3.5 must be converted to lift curves (C_l vs. α). These lift curves can then be used as input for the decambering method to calculate the wing lift

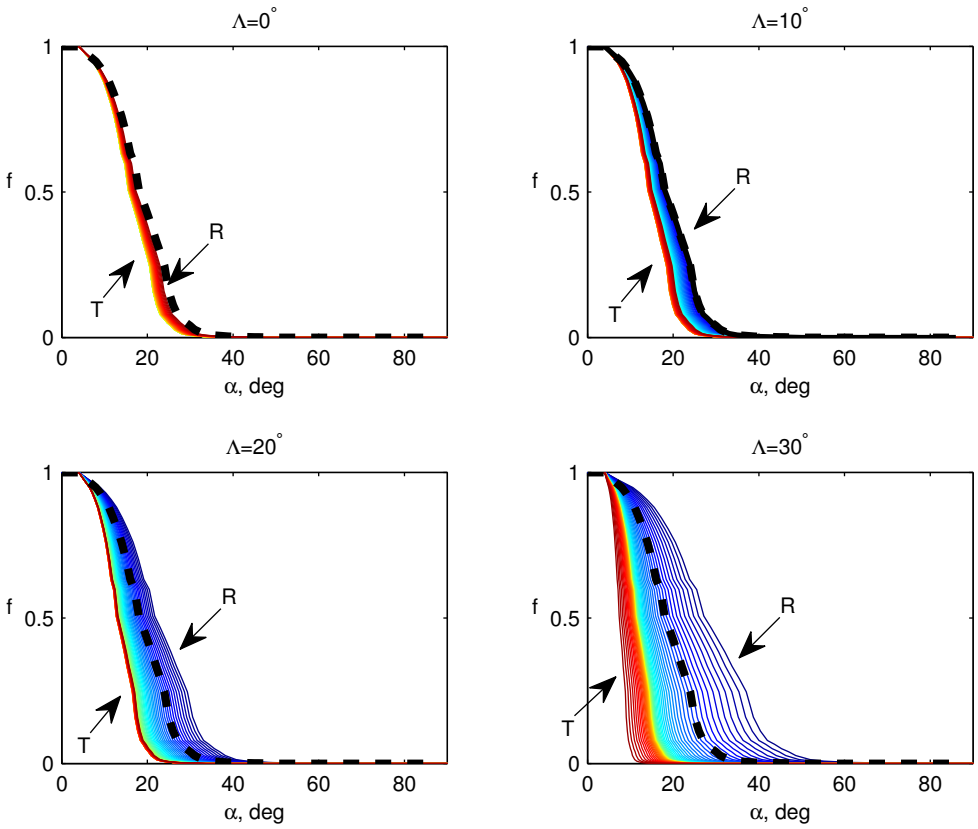

Figure 3.12: Scaled separation curves used to generate the input lift curves. The blue lines (R) depicting delayed separation represent the wing root and red lines (T) depicting advanced separation represent the wing tip. The dashed black line represents the airfoil separation curve

characteristics. The Beddoes-Leishman [55] model (Equations (3.12) – (3.13)) is used to relate the location of the separation point, f to the normal and chordwise forces, C_n and C_c, on the section.

$$C_n = a_0 \left(\frac{1 + \sqrt{f}}{2} \right)^2 \sin(\alpha - \alpha_{0L}) \tag{3.12}$$

$$C_c = a_0 \sin^2(\alpha - \alpha_{0L}) \sqrt{f} \tag{3.13}$$

$$C_l = C_n \cos(\alpha) - C_c \sin(\alpha) \tag{3.14}$$

Equation (3.14) then gives the lift coefficient on the wing section. Running these calculations for all sections of the wing for an array of angles of attack gives the lift characteristics of each section. The resulting C_l vs. α curves are shown in Figure 3.13. As expected, the sections of the rectangular wing have nearly identical lift curves, all of which are close to the 2-D lift curve. As the sweep angle increases, the root stalls at a higher angle of attack, with a corresponding increase in $C_{l,max}$. The opposite effect is seen at the wing tip, with stall occurring at a smaller angle of attack, resulting in a lower $C_{l,max}$.

An interesting observation here is that the modified airfoil curves do not resemble the CFD curve for very high angles of attack ($\alpha > 40°$). This is an effect of the model used to recreate the lift curves from the separation curves. At such high α, the separation point is at the leading edge, i.e. the flow over the airfoil is fully separated. The Beddoes method models the normal force in this region as $C_n = 0.25\ a_0\ \sin(\alpha)$, and the chordwise force as zero. This is why the lift curve resembles a sine curve when the separation has reached the leading edge. The Viterna model [57] could be a better fit for calculating the lift at such high angles of attack. However, it has not been implemented in the current work since the scope at this time extends only to the stall and near-post-stall regimes ($\alpha \leq 25°$).

3.7 Summary

In this chapter, the methodology used to extend the NCSU decambering approach to swept wings was presented. The process involves modifying the input lift characteristics of the wing sections to better represent the actual characteristics on swept wings. This is done indirectly, by modifying the separation characteristics and using these to calculate lift characteristics, because we know that the separation point location, f, is a monotonically decreasing function of the angle of attack, α, and is bounded between the trailing edge ($f = 1$) at low α and the leading edge ($f = 0$) at high α.

The modification applied to airfoil separation curve to obtain the section separation curves is a simple scaling transformation, which is a depends on α_s, the angle of attack at which the

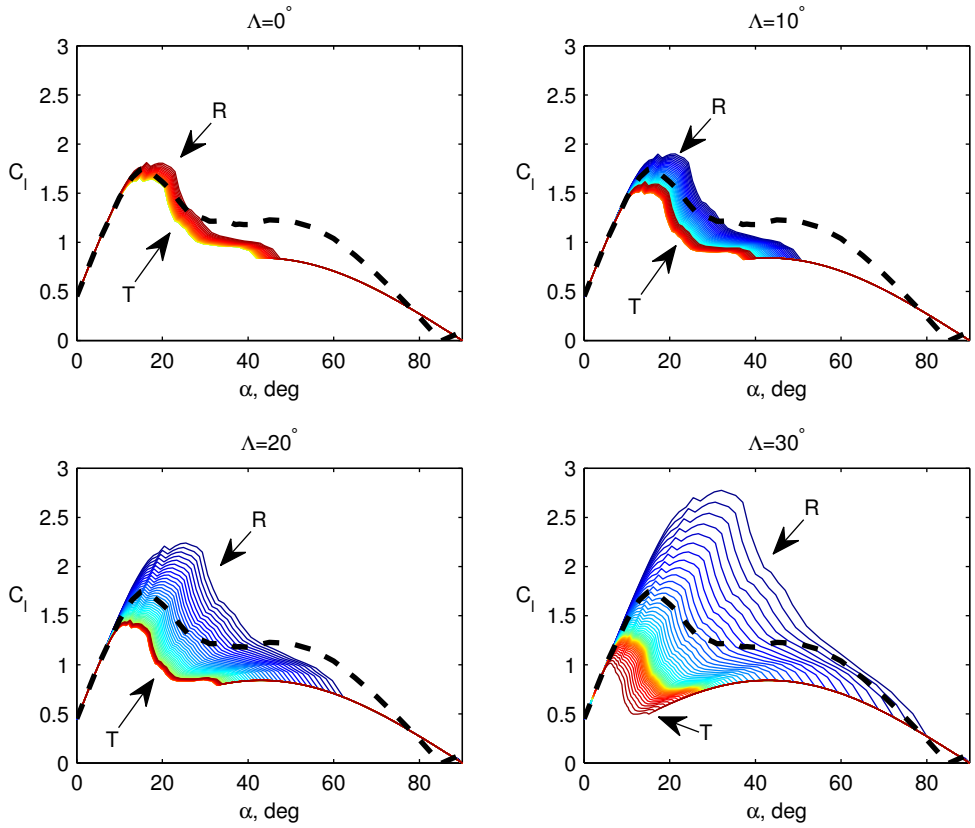

Figure 3.13: Lift curves for input to the VLM. Blue lines, depicting a higher $C_{l,max}$, depict the wing root (R) and red lines depicting a lower $C_{l,max}$, represent the wing tip (T). The dashed black line represents the airfoil separation curve

separation at the section reaches 50% of the chord, and α_1, the angle of attack at which the flow over the airfoil just starts separating. This parameter, α_1, is a constant for any given airfoil, while α_s varies with the sweep angle of the wing and the spanwise location of the section under consideration.

The values of α_s were initially obtained through raw data extracted from the CFD database, by parsing the flow-field at each section at each α for shear-stress reversal, but it was seen that the variation of α_s with spanwise location could be approximated to a cubic polynomial curve. The α_s actually used to generate the modified separation and hence lift curves were obtained from these polynomials to eliminate the effects of outliers caused by local discontinuities.

The Beddoes-Leishman model was used in two places: first to find the actual operating α of the sections at the wing, and second to convert the separation curves to lift curves for input to the decambering method.

The modified separation curves obtained from the algorithm described were shown to be representative of the actual separation behavior of the sections: delayed separation at inboard sections and advanced separation at outboard sections. As a result, the change in the lift characteristics was also seen: inboard sections stall at much higher C_l and α than the airfoil, while outboard sections stall at lower α, producing a smaller C_l.

Chapter 4

Results

The method described in Chapter 3 is executed and results are presented for four test wings, without decambering, and with decambering using airfoil data and modified section data as input. The test cases are wings of constant chord, with an aspect ratio of 12, and sweep angles of 0°, 10°, 20°, and 30°.

Results for the wing lift coefficient, C_L and spanwise lift distribution, $C_l(y)$ are presented next for the four wings. Three sets of C_L vs. α results are presented, labeled as follows:

- **VLM**: The result from a traditional VLM, without any corrections to account for separation and stall. This is equivalent to a potential flow simulation.
- **VLM - A**: The result from the VLM + decambering, using the 2-D lift curves as viscous input, and Scheme D as presented in Ref. [39].
- **VLM - M**: The result from the VLM + decambering, using modified lift curves as described in Chapter Chapter 3, and Scheme D from Ref. [39].

4.1 Wing lift coefficient

Figure 4.1 shows the change in wing lift coefficient, C_L with angle of attack, α for the three methods described above. The airfoil C_l vs. α curve is plotted as a reference.

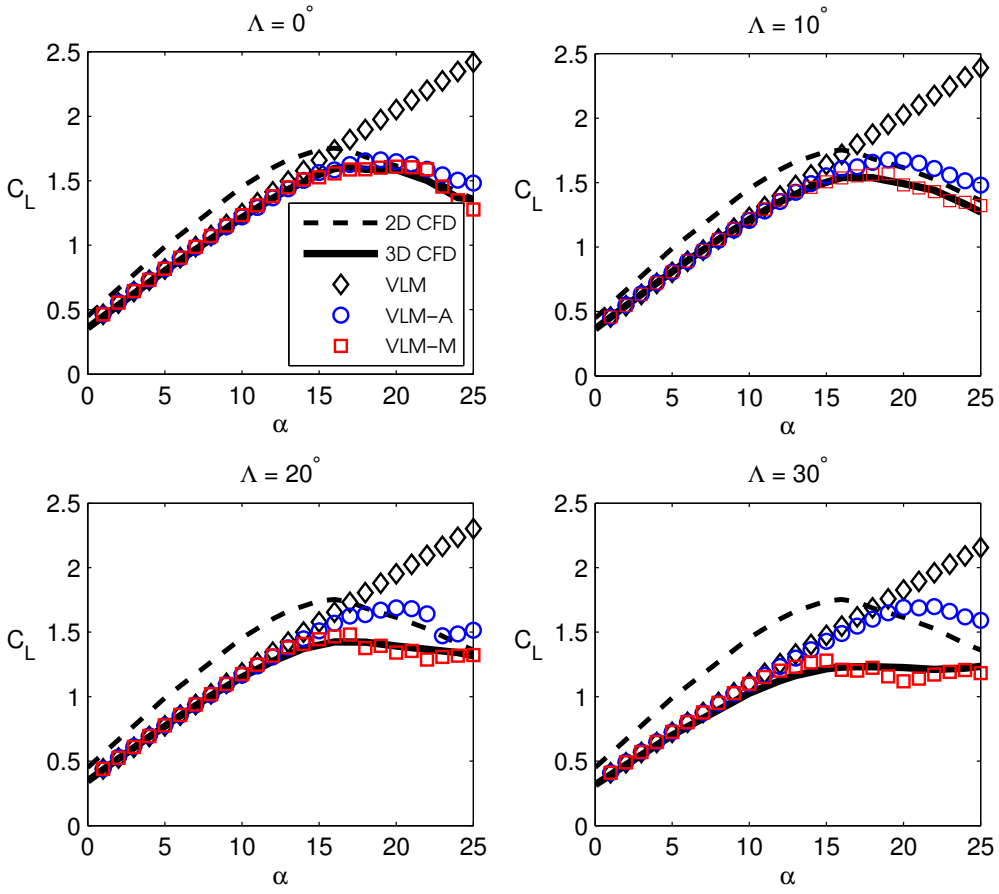

Figure 4.1: Lift curves for the wings with sweep angles $\Lambda = 0°$, $10°$, $20°$, and $30°$. The solid black line represents the values obtained from RANS CFD solutions, and the symbols represent the predictions of the three methods described above. The 2D airfoil lift curve (dashed black line) is also shown for reference

At low angles of attack, all three methods match the CFD results well, for all sweep angles. Additionally, $C_{L,\alpha}$, the slope of the lift curve, is also reasonably predicted by the methods for all sweep angles. As the angle of attack is increased, the boundary layer thickens and the lift generated by the wing deviates from the straight line predicted by the traditional VLM. The VLM - A method, for the unswept wing, is still able to predict the C_L fairly well, but, with increasing sweep, and the resulting spanwise flow, this method does not capture the deviation

from the potential flow solution. The method described in this paper returns accurate results at and beyond stall, upto the α studied.

4.2 Spanwise lift distribution and separation location

Figures 4.2 – 4.5 show the spanwise distributions of C_l as predicted by CFD, VLM-A, and VLM-M and the CFD-predicted f for the four wings. Also shown are the spanwise variations in the effective angle of attack, α_{eff} as predicted by CFD, VLM-A, and VLM-M. For each wing, the distributions are presented for $\alpha = 4$, 20, and 24 degrees. These three angles of attack were chosen to be representative of unstalled, near-stall, and post-stall flight conditions.

Examining the results for $\alpha = 4$ degrees first, it is seen that all four wings have fully-attached flow ($f = 1$) over the entire span, which is to be expected at this low angle of attack. At this angle of attack, the predicted C_l distributions from the three methods agree with each other excellently.

At $\alpha = 20$ degrees, all four wings are at an angle of attack just greater than their respective stall angles of attack. The rectangular wing results show that stall onset is at the root of the wing, where the separation has progressed to the mid-chord location and CFD shows a drop in the C_l distribution. With increasing sweep, the stall onset is seen to move towards the tip, with the root regions remaining unstalled (f close to 1) and the tip regions evincing flow separation. The swept wings show a distinct drop in CFD-predicted C_l over the outboard portions of the wings. For this angle of attack, the $C_l(y)$ predicted by VLM-A agrees with CFD predictions only for the unswept wing. In contrast, the VLM-M results for $C_l(y)$ agree well with CFD predictions for all four wings. At this angle of attack, the effect of decambering is visible – the method predicts an increased effective angle of attack at some sections so that the drop in lift at these sections reflects the stall behavior of the wing.

At $\alpha = 24$ degrees, all four wings are a post-stall condition. On all four wings, separation has progressed almost to the leading edge over most of the span, with the separation being biased toward the root for the unswept wing and towards the tips for the swept wings. This tipward

shift of stall from unswept to swept wings is reflected in the $C_l(y)$ prediction from CFD as well. The agreement with CFD is very good for the VLM-M method and comparatively poor for the VLM-A method, especially for the 30-degree sweep wing. The spanwise α_{eff} distribution plots show both VLM-A and VLM-M methods force some sections of the wing into the post-stall regime by calculating a high effective angle of attack. For the unswept wing, this region of high α_{eff} is near the root, showing that stall begins at the root. For the swept wings, this region of high effective α is, as expected, moved outboard, causing the wings to stall at the tips first. These results confirm that use of the modified section lift curves as input to the decambering approach is successful in reproducing the stall characteristics of swept wings.

It is seen that in some cases, especially at high angles of attack, the α_{eff} distribution calculated by the VLM-A method matches CFD predictions better than that of the VLM-M method. However, since the VLM-A method does not account for the change in lift distribution due to spanwise boundary layer transport on swept wings, a matching α_{eff} distribution does not necessarily translate to a correct C_l distribution, as is evident from Figures 4.2 – 4.5 below.

It is also seen that some spanwise lift distributions and calculated effective angle of attack distributions exhibit spanwise "sawtooth variations", even though the solutions are fully converged. Such spanwise sawtooth variations have also been observed by other researchers [39, 26, 24, 22, 25, 58]. This behavior is seen because the decambering trajectory lines for some spanwise stations intersect the input C_l–α curve at points beyond stall, whereas some trajectory lines intersect the input curve at points before stall. An illustration of this is seen in Figure 4.6. The figure shows the input lift curves for two adjacent spanwise stations on the 30° swept wing at an angle of attack of 24°. At station A ($2y/b = 0.725$), the solution has converged to the stalled region, with $\alpha_{eff} = 39.15°$, denoted by the red circle. At section B ($2y/b = 0.775$), denoted by the blue square, the solution has converged to in the unstalled region, with $\alpha_{eff} = 5.79°$. It has been speculated [38] that these sawtooth variations might be non-physical and an artifact of the numerical method. The sawtooth behavior of the spanwise lift distribution is a result of the oscillations in the calculated α_{eff}.

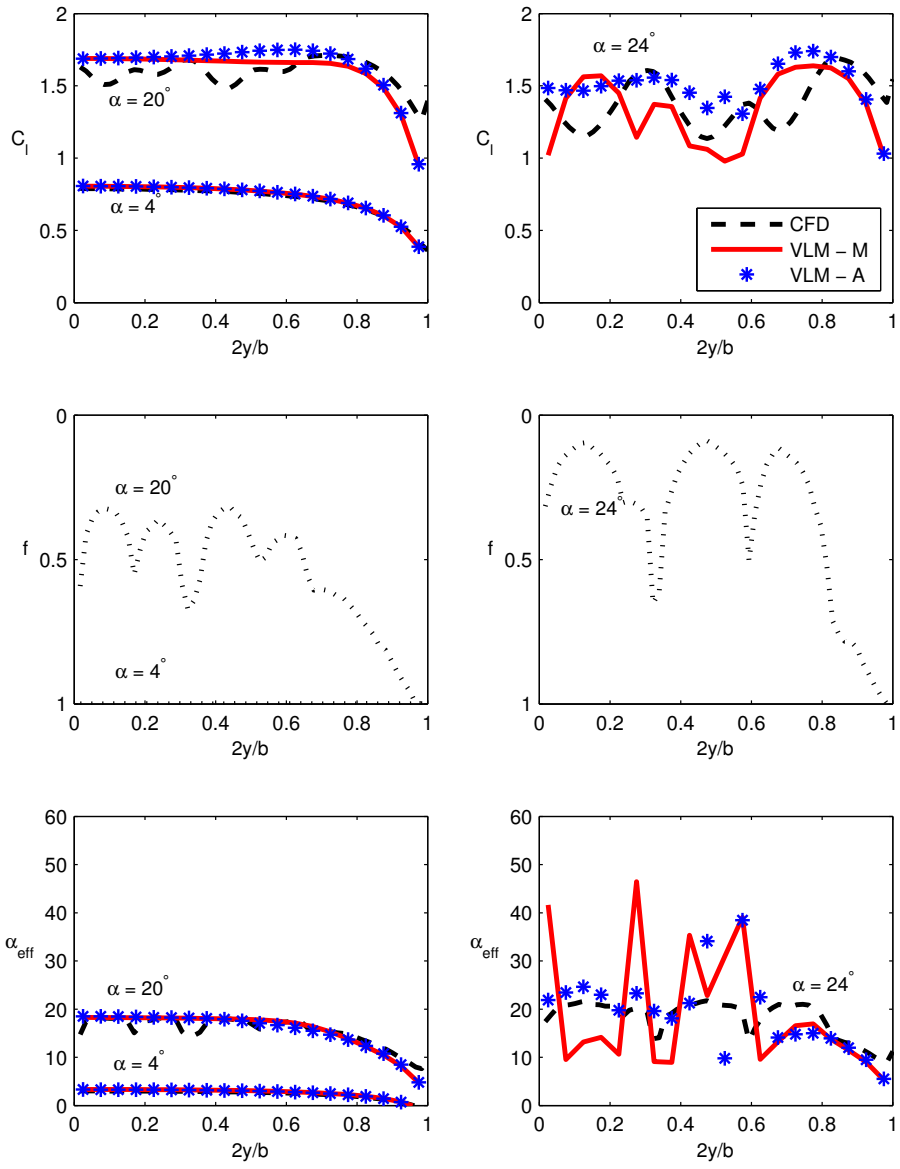

Figure 4.2: Spanwise lift distribution (top) and separation point location (bottom) for the rectangular wing

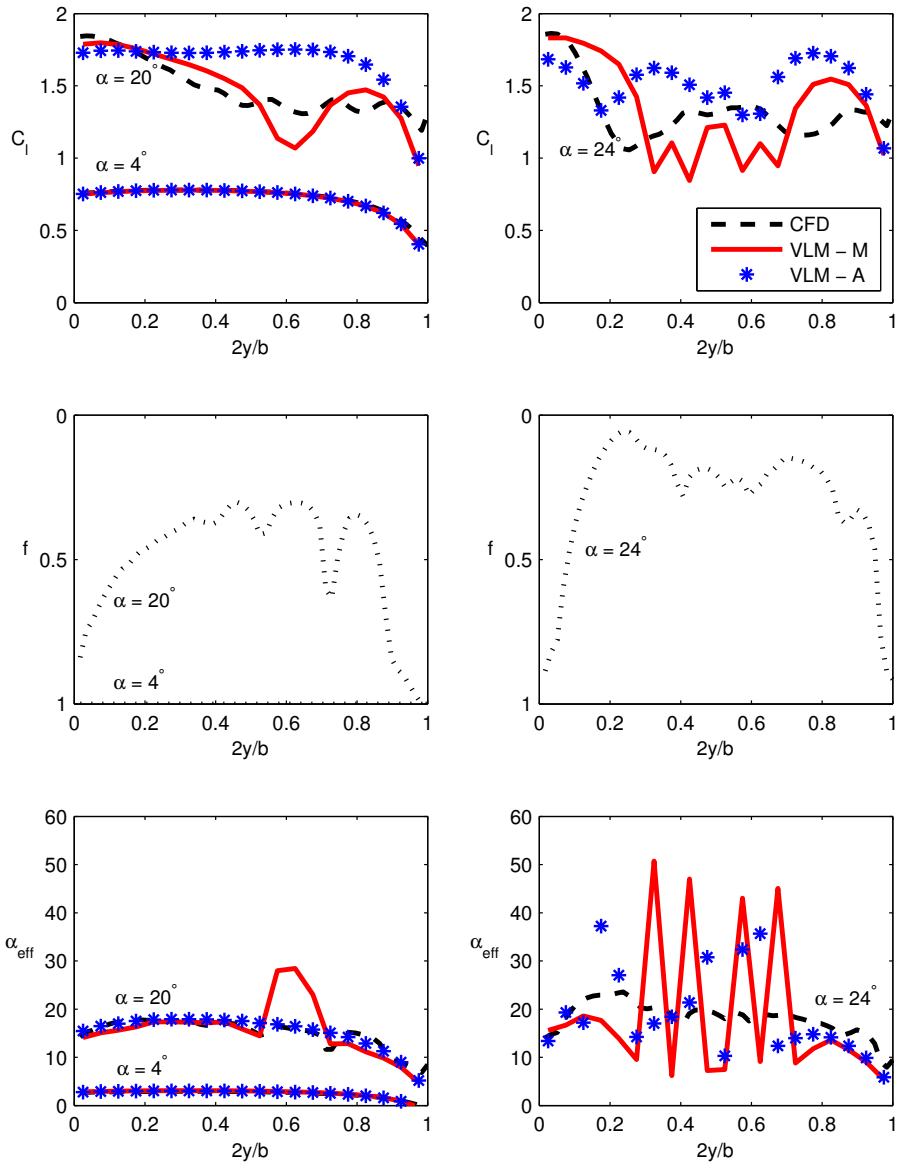

Figure 4.3: Spanwise lift distribution (top) and separation point location (bottom) for the 10 degree swept wing

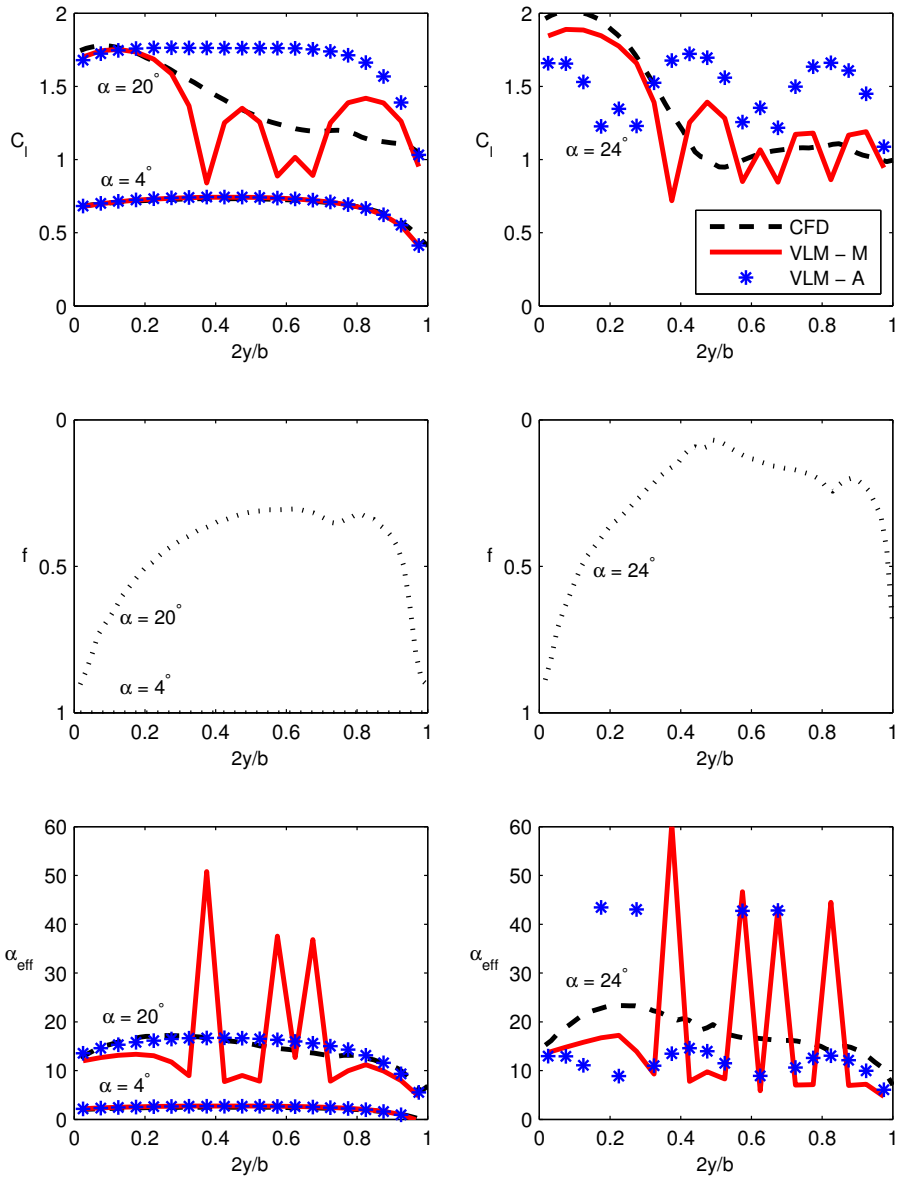

Figure 4.4: Spanwise lift distribution (top) and separation point location (bottom) for the 20 degree swept wing

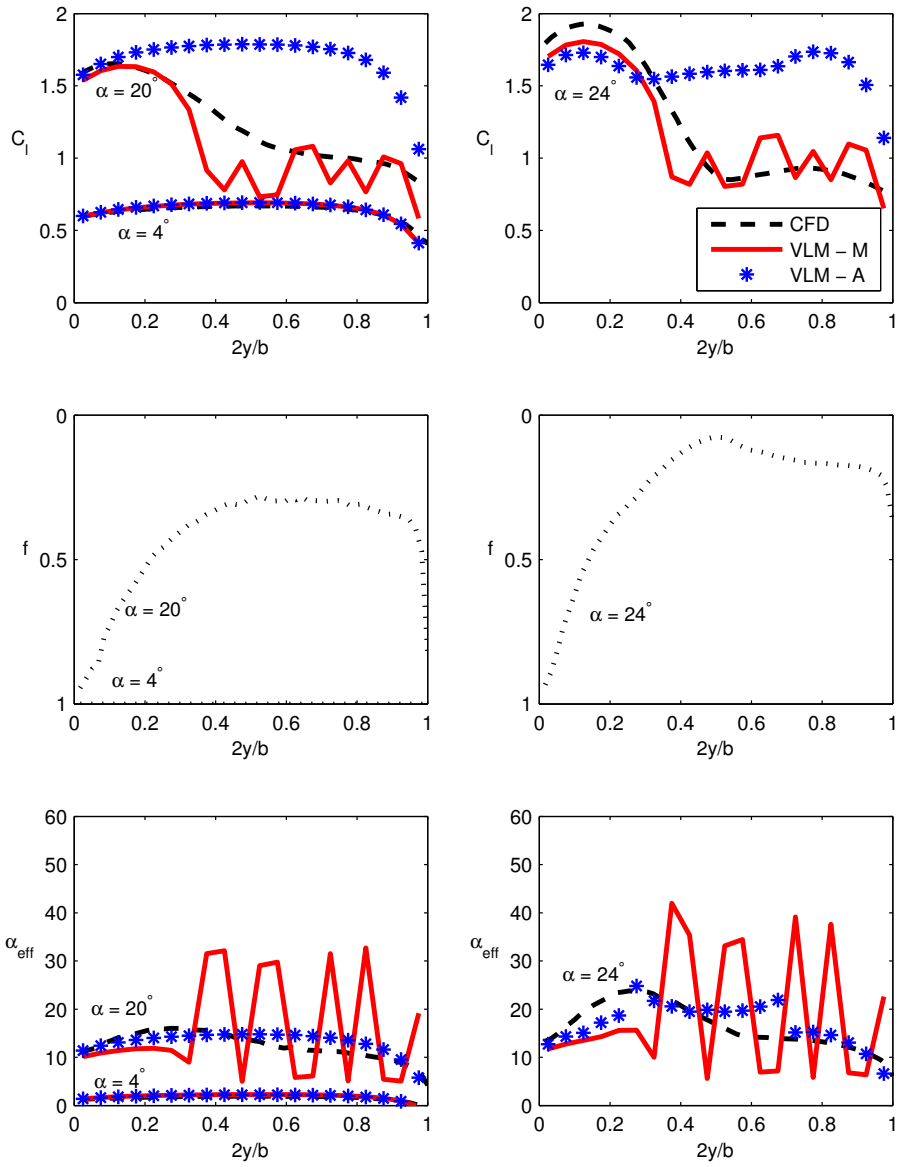

Figure 4.5: Spanwise lift distribution (top) and separation point location (bottom) for the 30 degree swept wing

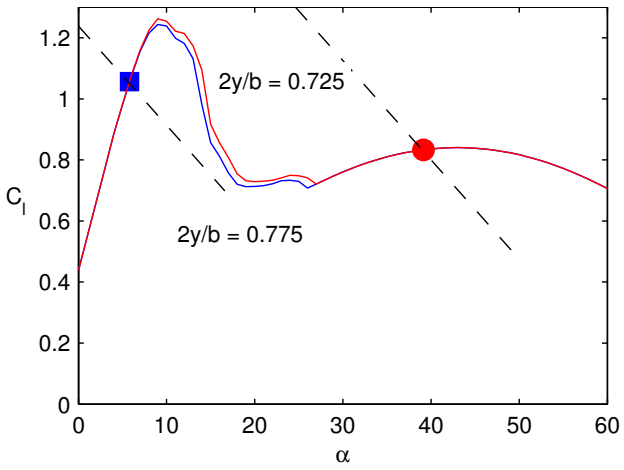

Figure 4.6: Converged operating points for adjacent stations at 72.5% and 77.5% of semi-span on the 30° swept wing at $\alpha = 24°$.

Chapter 5

Conclusions

This thesis presents the research related to development of a modification to NCSU's low-order method to extend the method to swept wings operating in the near-stall and post-stall region. The methodology presented corrects known shortcomings in utilizing the iterative decambering method to predict the stall characteristics of swept wings.

The iterative decambering method has conventionally been applied using viscous airfoil lift curves as input for all sections of the wing across the span. This approach yields reasonable results when the flow is more or less locally two-dimensional, and the stall characteristics it predicts agree well with CFD. For swept wing geometries, however, pressure gradients in the spanwise direction induce flow in the spanwise direction, from the root to the tip. This tipward transport of the boundary layer, at high angles of attack, modifies the stall characteristics of individual sections along the span. The flow remains attached upto higher angles of attack in the inboard regions of the wing, and separates at lower angles of attack in the outboard regions. This non-uniform change of the stall characteristics means the assumption that the airfoil lift curve is a reasonable representation of the section characteristics is no longer valid, causing inaccurate prediction of the wing stall characteristics by the unmodified decambering method.

The methodology presented addresses this deficiency by modifying the section characteristics at the different spanwise sections by taking into account the true progression of separation over

each section in generating its individual characteristic curve. The separation behavior at the sections can then be used to generate modified lift curves. These lift curves, while based on the airfoil lift curve, quantitatively describe the behavior of each wing section and account for the pressure-gradient-induced transport of the boundary layer. When these modified lift curves are used in place of the airfoil lift curves in the decambering approach, the results for C_L vs. α and C_l vs. y are seen to agree well with CFD predictions. While it has been known for several decades that tipward propagation of separated boundary layer on aft-swept wings is responsible for the stall behavior of these wings, the main contribution of the current work is in developing an approach to quantify this behavior and use this knowledge of the flow-physics in a numerical method.

The results presented in this thesis were obtained using the modified decambering approach for wings with a single (NACA4415) airfoil, and sweep angles of 0°, 10°, 20°, and 30°. Based on current results, a clear trend is seen in the sectional separation characteristics, and therefore section lift characteristics, as a function of sweep angle. These trends motivate further research to confirm that similar trends occur for a variety of airfoil and wing geometries.

Since full CFD results are required as an input to the methodology presented here, the method is a descriptive method. Further research could yield a predictive method, wherein the modifications to the airfoil lift curve could be determined without the need for full computational solutions.

5.1 Future work

5.1.1 Extending the CFD Database

In the immediate future, extending the CFD database will provide answers as to whether the method is applicable to a variety of wing shapes. Variation of wing shape could include parameters such as airfoil, sweep angle, taper, and aspect ratio. Additional CFD is also required to validate the method for more generalized wing geometries, like those with planform breaks

commonly found in transport aircraft.

5.1.2 Support for angular velocities and unsteady cases

Another avenue for research is to apply the method to cases with angular velocities — roll, pitch, and yaw. The presence of angular velocities changes the operating α of the sections, and this change is not necessarily uniform across the span. It would be interesting to see if the method can handle angular velocities by simply calculating the additional effective α due to the motion, or whether any modifications are necessary. This method could also be extended to predict stall in unsteady cases, using only steady CFD data as input. This would provide a significant cost-benefit over performing unsteady CFD calculations, which generally require require much more time or processing power than steady CFD calculations.

5.1.3 Physics-based predictive approach

The work described in this thesis has shown that modifying the viscous correction is a viable approach to extending the decambering to swept wings. However, the current approach is descriptive, not predictive, because these viscous corrections were obtained from full CFD results. The ultimate goal of this research is to develop a physics-based predictive model for any given geometry, based on flow-physics possibly obtained from surface parallel velocity components inside the low-order method.

REFERENCES

[1] P. Russell and J. Pardee. Final Report On the Accident on 1st June 2009 to the Airbus A330-203 Registerd F-GZCP Operated by Air France Flight AF 447 Rio de Janeiro - Paris. BEA FR, July 2012.

[2] Justin L. Petrilli. Reynolds-Averaged Navier-Stokes Computational Study of Various Wings and Airfoils Through Post-Stall Angles of Attack. Master's thesis, North Carolina State University, Department of Mechanical and Aerospace Engineering, 2013.

[3] J. Petrilli, R. Paul, A. Gopalarathnam, and N. Frink. A CFD Database for Airfoils and Wings at Post-Stall Angles of Attack. AIAA Paper 2013-2916, June 2013.

[4] P. Russell and J. Pardee. JSAT Loss of Control. Final Report - Commercial Aviation Safety Team (CAST), December 2000.

[5] Steven R. Jacobson. Aircraft Loss of Control Causal Factors and Mitigation Challenges. AIAA Paper 2010-0802, August 2010.

[6] Chris C. Critzos, Harry H. Heyson, and Robert W. Boswinkle Jr. Aerodynamic Characteristics of NACA 0012 Airfoil Section at Angles of Attack From 0° to 180°. NACA Technical Note 3361, January 1955.

[7] J. L. Tangler. Insight into Wind Turbine Stall and Post-stall Aerodynamics. *Wind Engineering*, 7:247–260, 2004.

[8] C. Lindenburg. Aerodynamic Airfoil Coefficients at Large Angles of Attack. IEA Symposium Paper ECN-RX–01-004, 2001.

[9] C. W. Harper and R. L. Maki. A Review of the Stall Characteristics of Swept Wings. NASA TN D-2373, 1964.

[10] C. Ostowari and D. Naik. Post Stall Studies of Untwisted Varying Aspect Ratio Blades with an NACA 4415 Airfoil Section—Part 1. *Wind Engineering*, 8(3):176–194, 1984.

[11] C. Ostowari and D. Naik. Post Stall Studies of Untwisted Varying Aspect Ratio Blades with an NACA 44XX Series Airfoil Sections—Part 2. *Wind Engineering*, 9(3):149–164, 1984.

[12] C. Ostowari and D. Naik. Post-Stall Wind Tunnel Data for NACA 44XX Series Airfoil Sections. Technical report, Solar Energy Research Institute, January 1985.

[13] Neal T. Frink, Shahyar Z. Pirzadeh, Harold L. Atkins, Sally A. Viken, and Joseph H. Morrison. CFD Assessment of Aerodynamic Degradation of Subsonic Transport Due to Airframe Damage. AIAA Paper 2010-500, 2010.

[14] Austin M. Murch and John V. Foster. Recent NASA Research on Aerodynamic Modeling of Post-Stall and Spin Dynamics of Large Transport Airplanes. AIAA Paper 2007-0463, 2007.

[15] Thomas L. Jordan, John V. Foster, Roger M. Bailey, and Christine M. Belcastro. AirSTAR: A UAV Platform for Flight Dynamics and Control System Testing. AIAA Paper 2006-3307, 2006.

[16] How X-Plane Works. `www.x-plane.com/desktop/how-x-plane-works/`. Accessed: 2014-06-25.

[17] Michael Selig. Modeling Full-Envelope Aerodynamics of Small UAVS in Realtime. AIAA Paper 2010-7635, August 2010.

[18] Paul E. Purser and M. Leroy Spearman. Wind-tunnel Tests at Low Speed of Swept and Yawed Wings Having Various Planforms. NACA Technical Note 2445, National Advisory Committee for Aeronautics, 1951.

[19] Lynn W. Hunton and Harry A. James. Use of Two-Dimensional Data in Estimating Loads on a 45-degree Sweptback Wing with Slats and Partial-span Flaps. NACA TN 3040, National Advisory Committee for Aeronautics, Ames Aeronautical Laboratory, Moffett Field, CA, November 1953.

[20] J. B. Tseng and C. Edward Lan. Calculation of Aerodynamic Characteristics of Airplane Configurations at High Angles of Attack. NASA CR 4182, 1988.

[21] C. P. van Dam, J. C. Vander Kam, and J. K. Paris. Design-Oriented High-Lift Methodology for General Aviation and Civil Transport Aircraft. *Journal of Aircraft*, 38(6):1076–1084, November–December 2001.

[22] John D. Anderson, Stephen Corda, and David M. VanWie. Numerical Lifting Line Theory Applied to Drooped Leading-Edge Wings Below and Above Stall. *Journal of Aircraft*, 17(12):898–904, 1980.

[23] Bruce Owens. Weissinger's Model of the Nonlinear Lifting Line Method for Aircraft Design. AIAA Paper 98-0597, January 1998.

[24] E. S. Levinsky. Theory of Wing Span Loading Instabilities Near Stall. AGARD Conference Proceedings No. 204, September 1976.

[25] Barnes W. McCormick. An Iterative Non-Linear Lifting Line Model for Wings with Unsymmetrical Stall. *SAE Transactions Paper No. 891020*, pages 91–98, 1989.

[26] S. T. Piszkin and E. S. Levinsky. Nonlinear Lifting Line Theory for Predicting Stalling Instabilities on Wings of Moderate Aspect Ratio. Technical report, General Dynamics Convair Report CASD-NSC-76-001, June 1976.

[27] R. S. Schairer. *Unsymmetrical Lift Distributions on a Stalled Monoplane Wing*. PhD thesis, 1939.

[28] W. R. Sears. Some Recent Developments in Airfoil Theory. *Journal of The Aeronautical Sciences*, 23:490–499, May 1956.

[29] J. C. Sivells and R. H. Neely. Method for Calculating Wing Characteristics by Lifting-Line Theory Using Nonlinear Section Lift Data. NACA TN 1269, April 1947.

[30] Itiro Tani. A Simple Method of Calculating the Induced Velocity of a Monoplane Wing. Rep. No. 111 (vol. 9, 3), Aero. Res. Inst., Tokyo Imperial Univ., August 1934.

[31] Adam M. Wickenheiser and Ephrahim Garcia. Extended Nonlinear Lifting-Line Method for Aerodynamic Modeling of Recongurable Aircraft. *Journal of Aircraft*, 48(5):1812–1816, September–October 2011.

[32] Ira H. Abbott and Albert E. von Doenhoff. *Theory of Wing Sections*. Dover, New York, 1959.

[33] Dieter Althaus and Franz Xaver Wortmann. *Stuttgarter Profilkatalog I*. Friedr. Vieweg & Sohn, Braunschweig, 1981.

[34] Michael S. Selig, James J. Guglielmo, A. P. Broeren, and P. Giguère. *Summary of Low-Speed Airfoil Data, Vol. 1*. SoarTech Publications, Virginia Beach, Virginia, 1995.

[35] Michael S. Selig, C. A. Lyon, P. Giguère, Cameron N. Ninham, and James J. Guglielmo. *Summary of Low-Speed Airfoil Data, Vol. 2*. SoarTech Publications, Virginia Beach, Virginia, 1996.

[36] C. A. Lyon, A. P. Broeren, P. Giguère, Ashok Gopalarathnam, and Michael S. Selig. *Summary of Low-Speed Airfoil Data, Vol. 3*. SoarTech Publications, Virginia Beach, Virginia, 1998.

[37] Mark Drela. XFOIL: An Analysis and Design System for Low Reynolds Number Airfoils. In T. J. Mueller, editor, *Low Reynolds Number Aerodynamics*, volume 54 of *Lecture Notes in Engineering*, pages 1–12. Springer-Verlag, New York, June 1989.

[38] Rinku Mukherjee and Ashok Gopalarathnam. Poststall Prediction of Multiple-Lifting-Surface Configurations Using a Decambering Approach. *Journal of Aircraft*, 43(3):660–668, May–June 2006.

[39] Ryan C. Paul and Ashok Gopalarathnam. Iteration Schemes for Rapid Post-Stall Aerodynamic Prediction of Wings Using a Decambering Approach. *International Journal for Numerical Methods in Fluids*, July 2014.

[40] Ashok Gopalarathnam, Ryan Paul, and Justin Petrilli. Aerodynamic Modeling for Real-Time Flight Dynamics Simulation (Invited). AIAA Paper 2013-0969, January 2013.

[41] Neal T. Frink, S.Z. Pirzadeh, P.C. Parikh, and M.J. Pandya. The NASA Tetrahedral Unstructured Software System (TetrUSS). *The Aeronautical Journal*, 104(1040):491–499, 2000.

[42] S.Z. Pirzadeh. Three-Dimensional Unstructured Grids by the Advancing Layer Method. *AIAA Journal*, 33(1):43–49, 1996.

[43] William J. Fredericks, Kevin R. Antcliff, Guillermo Costa, Nachiket Deshpande, Mark D. Moore, Edric A. San Miguel, and Alison N. Snyder. Aircraft Conceptual Design Using Vehicle Sketch Pad. AIAA Paper 2010-658, 2010.

[44] S.Z. Pirzadeh. Unstructured Viscous Grid Generation by the Advancing-Layers Method. *AIAA Journal*, 32(8):1735–1737, 1994.

[45] R Lohner and P Parikh. Three-dimensional grid generation by the advancing front method. *International Journal for Numerical Methods in Fluids*, 8(10):1135–1149, 1988.

[46] Neal T. Frink. Tetrahedral Unstructured Navier-Stokes Method for Turbulent Flows. *AIAA Journal*, 36(11):1975–1982, 1998.

[47] P.R. Spalart and S.R. Allmaras. One-Equation Turbulence Model for Aerodynamic Flows. AIAA Paper 92-0429, 1992.

[48] Joseph Katz and Allen Plotkin. *Low-Speed Aerodynamics*. Cambridge Aerospace Series. Cambridge University Press, Cambridge, UK, second edition, 2001.

[49] Rinku Mukherjee, Ashok Gopalarathnam, and SungWan Kim. An Iterative Decambering Approach for Post-Stall Prediction of Wing Characteristics Using Known Section Data. AIAA Paper 2003-1097, January 2003.

[50] R. Paul and A. Gopalarathnam. Simulation of Flight Dynamics with an Improved Post-Stall Aerodynamics Model. AIAA Paper 2012-4956, August 2012.

[51] A. Gopalarathnam, R. Paul, and J. Petrilli. Aerodynamic Modeling for Real-Time Flight Dynamics Simulation. AIAA Paper 2013-0969, January 2012.

[52] Joseba Murua, Rafael Palacios, and J. Michael R. Graham. Applications of the unsteady vortex-lattice method in aircraft aeroelasticity and flight dynamics. *Progress in Aerospace Sciences*, 55:46–72, 2012.

[53] Allen E. Winkelmann and Jewell B. Barlow. Flowfield Model for a Rectangular Planform Wing beyond Stall. *AIAA Journal*, 18(8):1006–1008, 1980.

[54] Steven A. Yon and Joseph Katz. Study of the Unsteady Flow Features on a Stalled Wing. *AIAA Journal*, 36(3):305–312, 1998.

[55] JG Leishman and TS Beddoes. A Semi-Empirical Model for Dynamic Stall. *Journal of the American Helicopter Society*, 34(3):3–17, 1989.

[56] Kristen N. Patrick. Boundary Layer and Flow Physics of Swept and Unswept Wings in Stall and Post-Stall Conditions from CFD Solutions. Master's thesis, North Carolina State University, Department of Mechanical and Aerospace Engineering, 2014.

[57] L.A. Viterna and D.C. Janetzke. Theoretical and experimental power from large horizontal-axis wind turbines. NASA TM NASA-TM-82944, National Aeronautics and Space Administration, Lewis Research Center, Clevelend, OH, 1982.

[58] S. Gallay and E. Laurendeau. Nonlinear Generalized Lifting-Line Coupling Algorithms for Pre/Poststall Flows. *AIAA Journal*, 53(7):1784–1792, April 2015.